J|A|C|S

Cite This: *J. Am. Chem. Soc.* 2019, 141, 3217−3231

Article

pubs.acs.org/JACS

Microsolvation of the Redox-Active Tyrosine-D in Photosystem II: Correlation of Energetics with EPR Spectroscopy and Oxidation-Induced Proton Transfer

Abhishek Sirohiwal,[†,‡] Frank Neese,[†] and Dimitrios A. Pantazis*,[†]

†Max-Planck-Institut für Kohlenforschung, Kaiser-Wilhelm-Platz 1, 45470 Mülheim an der Ruhr, Germany
‡Fakultät für Chemie und Biochemie, Ruhr-Universität Bochum, 44780 Bochum, Germany

S *Supporting Information*

ABSTRACT: Photosystem II (PSII) of oxygenic photosynthesis captures sunlight to drive the catalytic oxidation of water and the reduction of plastoquinone. Among the several redox-active cofactors that participate in intricate electron transfer pathways there are two tyrosine residues, Y_Z and Y_D. They are situated in symmetry-related electron transfer branches but have different environments and play distinct roles. Y_Z is the immediate oxidant of the oxygen-evolving Mn_4CaO_5 cluster, whereas Y_D serves regulatory and protective functions. The protonation states and hydrogen-bond network in the environment of Y_D remain debated, while the role of microsolvation in stabilizing different redox states of Y_D and facilitating oxidation

or mediating deprotonation, as well the fate of the phenolic proton, is unclear. Here we present detailed structural models of Y_D and its environment using large-scale quantum mechanical models and all-atom molecular dynamics of a complete PSII monomer. The energetics of water distribution within a hydrophobic cavity adjacent to Y_D are shown to correlate directly with electron paramagnetic resonance (EPR) parameters such as the tyrosyl g-tensor, allowing us to map the correspondence between specific structural models and available experimental observations. EPR spectra obtained under different conditions are explained with respect to the mode of interaction of the proximal water with the tyrosyl radical and the position of the phenolic proton within the cavity. Our results revise previous models of the energetics and build a detailed view of the role of confined water in the oxidation and deprotonation of Y_D. Finally, the model of microsolvation developed in the present work rationalizes in a straightforward way the biphasic oxidation kinetics of Y_D, offering new structural insights regarding the function of the radical in biological photosynthesis.
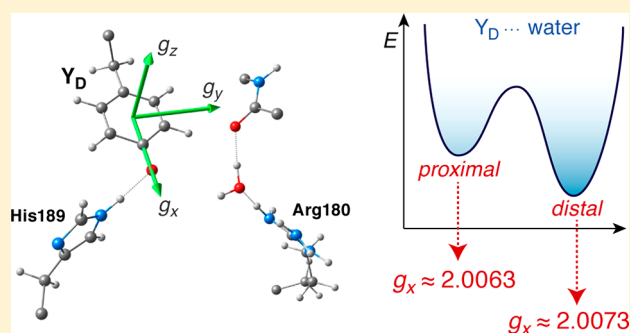
■ INTRODUCTION

Photosystem II (PSII) is the primary enzymatic complex in oxygenic photosynthesis. It uses the energy of sunlight to drive the oxidation of water to dioxygen and the reduction of a mobile plastoquinone, which carries reducing equivalents further along the photosynthetic chain to be eventually used in carbon fixation.[1,2] PSII contains several redox-active cofactors that sustain a complex network of electron transfer pathways, which play both productive and protective roles (Figure 1).[3] Among the redox-active components of PSII are the two tyrosine residues D1-Tyr161 (Y_Z) and D2-Tyr160 (Y_D).[4−7] Y_Z is interacting directly with the water oxidation site of PSII, the oxygen-evolving complex (OEC).[8,9] The chlorophyll-containing primary charge separation site[10] of the enzyme ($P_{680}^{•+}$) oxidizes Y_Z, and the resulting tyrosyl radical functions in turn as the immediate oxidant of the tetramanganese−calcium (Mn_4CaO_5) cluster of the OEC that catalyzes water oxidation.[11−15] The other redox-active tyrosine, Y_D, is located in the symmetric electron transfer branch of PSII that is not active in water oxidation.[16,17]

Although Y_D does not participate in the mainstream electron transfer processes, it plays important regulatory roles for the smooth and efficient functioning of PSII.[17−23] Despite the large distance between Y_D and the OEC (ca. 30 Å), it is crucial for modulating the various S_i oxidation states ($i = 0−4$)[24] of the Mn_4CaO_5 cluster of the OEC.[18,19,25,26] Y_D is oxidized on a time scale of seconds by the OEC in its S_2 or S_3 state,[19,26−28] while Y_D-$O^•$ can be reduced by the S_0 state during dark adaptation,[20,21] both processes aiding the OEC to reach the dark-stable S_1 state. In addition, Y_D is proposed to enhance the rate of electron transfer at the Y_Z site by specific electrostatic interaction with $P_{680}^{•+}$.[22,29−32]

The two tyrosine residues have different properties, as Y_Z exhibits fast oxidation and reduction kinetics, whereas Y_D displays slower oxidation and reduction rates at physiological pH.[33] The $Y_Z^•$ radical is short-lived and decays with a $t_{1/2}$ of 0.03−1 ms,[34−37] whereas $Y_D^•$ decays with a $t_{1/2}$ in the range of
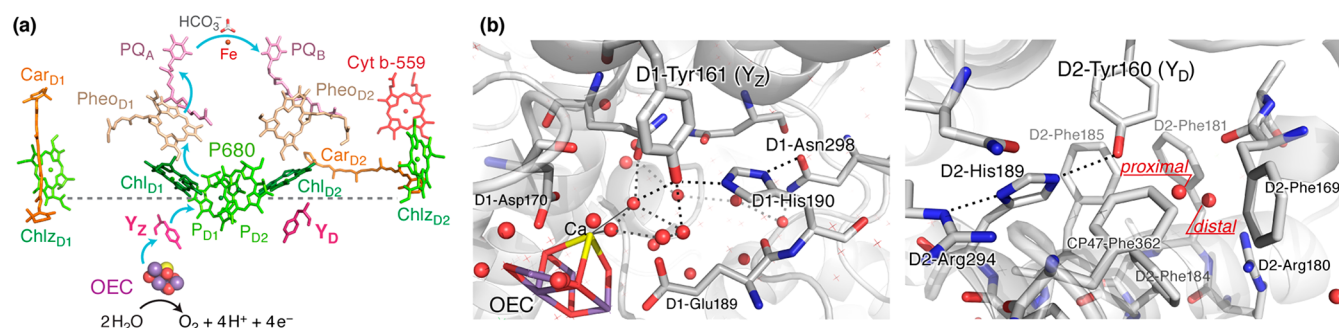
Figure 1. (a) Important redox-active cofactors of photosystem II involved in charge separation, electron transfer, and catalysis. The blue arrows indicate the physiological electron flow from water to the plastoquinone acceptor. (b) Comparison of the immediate environment of the two redox-active tyrosine residues, Y_Z (left) and Y_D (right). Coordinates are obtained from the 1.9 Å resolution crystallographic model of PSII[8] (PDB ID: 3WU2).

minutes to hours.[33] Additionally, they have different estimated redox potentials, i.e., +900−1000 mV for Y_Z[19] and +700−800 mV for Y_D.[19,33] Looking at the immediate environment for potential structural explanations of these divergent properties, it becomes obvious that the two residues have clear similarities but also important differences. Both tyrosines have a hydrogen-bonded histidine partner, D1-His190 for Y_Z and D2-His189 for Y_D. D1-His190 is further hydrogen-bonded to D1-Asn298,[38] while D2-His189 to D2-Arg294. A fundamental difference is that whereas Y_Z is embedded in a water-rich hydrogen-bonding network, which includes waters directly coordinated to the calcium ion of the OEC cluster, Y_D is situated at a hydrophobic phenylalanine-rich cavity that in recent crystallographic models appears to accommodate a single water molecule confined between Y_D and an arginine−aspartate pair, D2-Arg180−Asp333. Two water positions have been identified in some, but not all, crystallographic models.[8,9,39−43] These are termed proximal (at a hydrogen-bonding distance of ca. 2.7 Å from the phenolic oxygen of Y_D) and distal (at a distance of >4.0 Å from the phenolic oxygen). Understanding the effect of micro-solvation and the role of the histidine partner and the confined water is fundamental for understanding the mechanism of formation of the Y_D radical, its spectroscopic properties and differences from Y_Z, the possible proton translocation pathways, and ultimately the functional role of Y_D in the context of biological photosynthesis.

A fundamental question is whether deprotonation proceeds with the same mechanism in both tyrosine sites upon oxidation or not. Two contrasting ideas exist in the literature. The first is that Y_D follows the same mechanism as Y_Z,[44−49] for which it is rather well established that the phenolic proton simply shifts toward the His partner upon oxidation and is available to return for fast reduction of the $Y_Z^\bullet$ radical. This has been traditionally assumed to be the case with the Y_D−His189 pair and guided the interpretation of experimental data and past modeling of the system. The second idea is that proton transfer in Y_D follows an entirely different mechanism;[50−55] however on this point diverging views exist[56,57] and the available data are structurally ambiguous. Even before the crystallographic confirmation of the presence of a water molecule near Y_D, there were reports supporting the presence of one or more coupled water molecules or exchangeable protons near Y_D.[44,58−63] For example, the electron paramagnetic resonance (EPR) spectrum[64] of oxidized Y_D in His189Gln mutants is characteristic of a neutral tyrosyl radical with no hydrogen bond, suggesting the existence of a proton acceptor other than His189. Similar conclusions were reached from FTIR studies.[65] Even more intriguingly, based on a proton inventory study Barry and co-workers[66,67] reported on a multiproton donation pathway to the Y_D radical, suggesting that water plays a crucial role in proton transfer to and from the Y_D site. Additionally, FTIR studies by Hienerwadel et al. suggested the presence of two proton exit channels[68] and claimed the observation of proton release to the membrane surface upon Y_D radical formation.[69,70] Currently it is not obvious how to cast all of these observations and interpretations into a unique and precise structural model.

The identification of the cavity water in recent crystallo-graphic models of PSII led to renewed discussions and speculations on its role and importance. This has been recently highlighted experimentally by Sjöholm et al.,[55] who employed continuous-wave EPR and two-pulse electron spin echo envelope modulation (ESEEM) spectroscopy to correlate the time of H/D exchange with the redox state of Y_D and suggested that the position of the water molecule might be relevant for interpreting their observations. Further studies[53,54] conjectured that the biphasic kinetics of Y_D oxidation may be related to the position of the water molecule in the hydrophobic cavity. Using computational simulations Saito et al.[50] suggested that the two water positions reflect a mechanism of water-mediated proton removal upon oxidation of the Y_D residue: it was suggested that the water molecule preferably occupies the proximal position, hydrogen bonding to the reduced Y_D residue, but abstracts the phenolic proton upon formation of $Y_D^\bullet$ and shifts to the distal position, releasing the proton outside the cavity with the involvement of Arg180. The above studies attribute functional significance to the presence of two crystallographic water positions, but the structural interpretations they propose are neither clear nor consistent with each other, while their agreement with all available data from crystallography and spectroscopy has not been explicitly examined.

A powerful way to clarify these open questions is to use quantum chemical methods in order to couple the detailed modeling of the Y_D environment with calculation of spectroscopic parameters for possible oxidized forms of Y_D in relation to protonation states and the position of the cavity water. EPR spectroscopy offers an invaluable source of electronic structure information and has been used extensively in the study of Y_D oxidation,[46,47,64,71−79] but the various observations have not received atomistic explanations in the context of current structural information. In the present work

we offer new insights into the mechanism of Y_D oxidation using extended quantum chemical models as well as all-atom force-field molecular dynamics modeling of PSII to understand the energetics of water distribution and to relate available EPR observations with specific structural models. Our results lead to a revised model regarding the role of microsolvation for the oxidation of the Y_D residue and suggest a coherent structure-based explanation of both the spectroscopic and the kinetic data reported for the Y_D radical of PSII.

■ METHODOLOGY

Molecular Dynamics Simulations. Classical molecular dynamics simulations were performed on the PSII monomer obtained from the 1.9 Å crystal structure (PDB ID: 3WU2)[8] to understand the stability and dynamics of the water molecule in the Y_D cavity under the influence of the protein environment. The protonation states of Y_D and the nearby residues were assigned manually. The AMBER03 force field[80] parameters were used for standard protein residues and ions, and the TIP3P water model[81] was employed for water molecules. Force-field parameters for the various cofactors were taken from the literature.[82,83] The PSII monomer was solvated with TIP3P water in a simulation box of dimensions 115.1 × 130.98 × 128.76 Å. Crystallographic waters were retained during system preparation, and counterions were added to maintain charge neutrality. The final system consists of 428 890 atoms. Energy minimization to remove the structural bad contacts included 2000 steps of steepest descent followed by conjugate-gradient minimization. The solvent around the protein is well equilibrated using a force constant of 10 kJ mol^{-1} Å^{-2} on the heavy atoms (except hydrogens and oxygen of water) of the protein. The equilibration phase included NVT and NPT simulations performed for 100 ps at 300 K. A subsequent production run of 3000 ps (T = 300 K, P = 1 bar) was performed with a time integration step of 1 fs. C_α carbon atoms were restrained with a force constant of 100 kJ mol^{-1} Å^{-2} to avoid unnatural large-scale backbone movements due to absence of the membrane. The temperature and pressure were maintained using the Berendsen thermostat[84] and Parinello-Rahman barostat[85] with a coupling constant of 0.1 and 2.0 ps, respectively. The nonbonded interactions were treated explicitly up to 12 Å in the production run, and interactions above this cutoff were treated using the particle-mesh-Ewald (PME) summation algorithm.[86,87] The LINCS constraint algorithm[88] was employed for all bonds. The simulations were performed using the GROMACS software package (version 4.6.7).[89]

Quantum Cluster Models. The starting point for the quantum chemical simulations was the same crystal structure of PSII (PDB ID: 3WU2) from which we built quantum cluster models that encompass a large region of the protein around the Y_D residue (Figure 2). The model includes the D2 residues Ile159, Tyr160 (Y_D), Pro161, Leu162, Glu163, Gln164, Phe169, Ala170, Arg180, Phe181, Leu182, Leu183, Phe184, Phe185, Gln186, Gly187, Phe188, His189 (the H-bonding partner of Y_D), Asn292, Arg294, Asp333, Phe362, and Phe363, as well as the CP47 residues Phe362 and Phe363. The continuous chain fragment Arg180−His189 defines an α-helical region. The cavity that contains the water molecule is lined by hydrophobic residues Phe169, Phe181, Phe184, Phe185, and CP47-Phe362. The side chains of residues Ile159, Leu162, Leu182, Leu183, Gln186, Phe188, and CP47-Phe363 point to the exterior of the model; so for computational convenience in the final QM calculations they were terminated at the C_β atom, replaced by hydrogen. The total size of the final QM cluster model after addition of hydrogens and corrections for proper termination of peptide bonds is 301 or 302 atoms depending on the choice of protonation state.

For refining the structure of the QM model all hydrogen positions were first optimized by constraining non-hydrogen atoms in their crystallographic positions and freezing specific hydrogen atoms that replaced backbone atoms representing the directions of continuation of peptide chains. Following this initial cleanup of the model, the system was allowed to optimize with imposition of only C_α and C_β
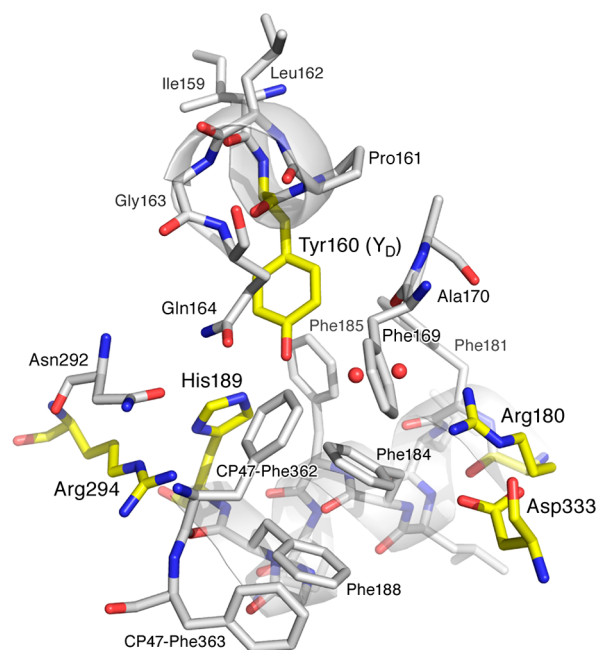

Figure 2. Residues considered for the construction of the QM cluster model used in the present work. The coordinates were obtained from PDB structure 3WU2. Both sites for the cavity water (red spheres) are shown, according to their crystallographic occupancies. Selected amino acid residues are labeled, all from the D2 protein of PSII unless otherwise indicated. The water cavity is defined by the side chain phenyl groups of Phe169, Phe181, Phe184, Phe185, and CP47-Phe362. The side outward-pointing chains of certain peripheral helix residues were simplified in the final QM calculations as described in the main text. The residues shown in yellow correspond to the fully relaxed part of the QM model.

constraints to maintain the protein folding effect. The system was divided into a relaxed active part and a part that is still treated fully quantum mechanically but where constraints are applied to heavy atoms. The constrained part includes most of the hydrophobic residues that define the hydrophobic cavity, while the relaxed part consists of Y_D, His189, Arg294, Arg180, Asp333, the backbone peptide bonds (CO-NH) of Phe169−Ala170 and Phe362−Phe363, the manually added hydrogens on C_α atoms of these residues, and the cavity water.

Computational Details. Geometry optimizations were performed with the PBE functional[90] using D3(BJ) dispersion corrections.[91,92] The Def2-TZVP basis sets[93] were used for all atoms in the fully optimized part, and the Def2-SVP[93] basis sets were used for atoms in the constrained part of the model. This combination led to a total number of 3477 basis functions. The resolution of identity (RI) approximation[94,95] was employed to speed up the calculations of Coulomb integrals, in combination with Weigend's universal Def2/J auxiliary basis sets.[96,97] The conductor-like polarizable continuum model (CPCM)[98] was employed with a dielectric constant of ε = 6 throughout the investigation. Single-point energy calculations on selected models were performed using the hybrid B3LYP[99] and the meta-hybrid TPSSh[100] functionals in conjunction with the larger Def2-TZVPP basis set (total of 6795 basis functions). EPR parameters of the tyrosyl radical in our models were calculated using the TPSSh functional with Barone's EPR-II basis set.[101] This approach has been shown to be reliable for the calculation of EPR parameters in various related systems (see also the Supporting Information for a brief comparison of functionals).[102−108] The chain-of-spheres approximation[109] was used in the evaluation of exchange integrals for the calculations employing hybrid functionals. Tight convergence settings were used throughout, along with higher than default integration grids (Grid6 and GridX6 in ORCA nomenclature).

The g-factors of tyrosyl radical models were computed within the framework of a DFT-based coupled-perturbed self-consistent field approach,[110] in conjunction with an efficient implementation of the spin−orbit mean-field approximation to the Breit−Pauli operator[111] for the spin−orbit coupling. The gauge origin for the computation of g-factors was chosen to be the center of the tyrosyl radical ring. The hyperfine coupling constants calculations were performed for the protons present on the $Y_D^{\bullet}$ radical ring, on the C_β carbon, and also for protons that are directly hydrogen-bonded to the $Y_D^{\bullet}$ radical, His-$N_\epsilon H$ and H_2O. We have also computed the hyperfine coupling constants for the ^{13}C nuclei and the ^{17}O of Y_D, as well as of the ^{15}N of His189. All quantum chemical calculations were performed with ORCA.[112,113]

■ RESULTS

Analysis of Crystallographic Models. Table 1 collects representative data from crystallographic models of PSII (see

Table 1. Distances between the O Atom of Y_D and the O Atom of the Cavity Water That Can Be Assigned to Either the Proximal or the Distal Position[a]

PDB	organism	resolution (Å)	$O_{YD}...O_{prox}$ (Å)	$O_{YD}...O_{dist}$ (Å)	ref
5MX2	T. elongatus	2.55		4.0	40
5MX2	T. elongatus	2.55		3.9	40
5H2F	T. elongatus	2.2		4.4	41
5H2F	T. elongatus	2.2		4.3	41
4IL6	T. vulcanus	2.1		4.3	42
4IL6	T. vulcanus	2.1		4.1	42
4UB6	T. vulcanus	1.95	2.7 (0.40)	4.5 (0.60)	9
4UB6	T. vulcanus	1.95	3.1 (0.65)	4.5 (0.35)	9
4UB8	T. vulcanus	1.95	2.6 (0.35)	4.3 (0.65)	9
4UB8	T. vulcanus	1.95	2.7 (0.40)	4.5 (0.60)	9
3WU2	T. vulcanus	1.9	2.9 (0.5)	4.4 (0.5)	8
3WU2	T. vulcanus	1.9		4.4	8
6DHP[b]	T. elongatus	2.04		4.5	114
6DHP	T. elongatus	2.04		4.4	114

[a]Two entries per structure are provided, corresponding to each one of the PSII monomers. When both proximal and distal water sites are occupied, the numbers in parentheses correspond to crystallographic occupancies for the O atom. [b]From the S_0 state enriched sample; see Table S1 for complete data.

Table S1 for a complete collection of data).[8,9,39−43,114] The absence of a proximal water in many cases, the distribution of distances between the phenolic oxygen of Y_D and the cavity water, and the relative occupancies of the two water positions when both sites are modeled as occupied in the refinement of the crystallographic data suggest that the distal water position can be considered the dominant/majority form. It is likely that the distribution of water between proximal and distal positions correlates with the oxidation state of Y_D in the samples, but it is not possible to confirm the oxidation state of Y_D in all cases or the percentage of centers containing a $Y_D^{\bullet}$ radical. Therefore, no such correlation can be deduced by inspection of available crystallographic models. Nevertheless, EPR measurements performed on the same samples used for a recent crystallographic model (5MX2) of OEC-depleted PSII that has only a distal water in both monomers showed no Y_D radical signal; that is, Y_D was reduced in these samples.[40] This suggests, in contrast to the computational study of Saito et al.,[50] that the distal water position might be more stable compared to the proximal position *irrespective* of the redox state of the Y_D residue.

Therefore, the problem of Y_D microsolvation needs to be revisited with refined energetics obtained using expanded models. Additionally, it is necessary to seek connections with spectroscopic data, particularly the EPR spectra of the radical, which we accomplish as described in the following by explicit computation of the tyrosyl g-tensor for a series of possible structural models.

Energetics of Cavity Water Distribution in the Reduced State. Various protonation states and patterns along with different positions and orientations of the cavity water were explored with QM cluster calculations. We single out three models for further discussion and analysis as representative of the major species obtained as stable minima under the assumption of a neutral (Y_D-OH) tyrosine residue (Figure 3). In models 1_R and 2_R (the subscript "R" is used to denote the reduced state of Y_D) the protonation of the N_δ (or
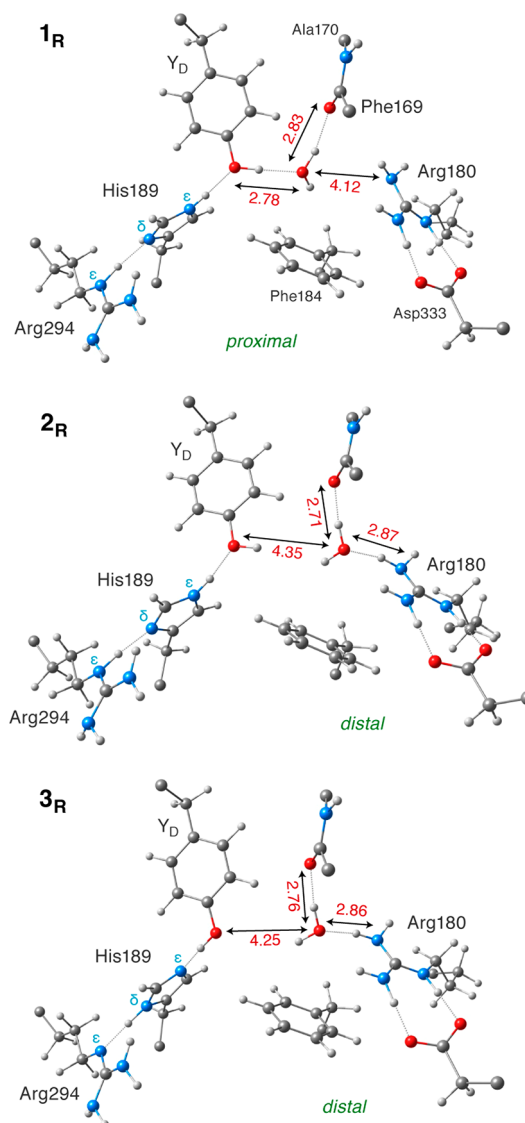

Figure 3. Depiction of the central region extracted from three optimized QM models with reduced Y_D, featuring different proton arrangements in the Arg294−His189−Y_D triad and different positions of the cavity water. Selected distances are indicated (in Å) between the O atom of the cavity water, the O atom of Y_D, the O atom of the Phe169 peptide carbonyl, and the N_η atom of the NH_2 group of Arg180 that interacts with water at the distal position.
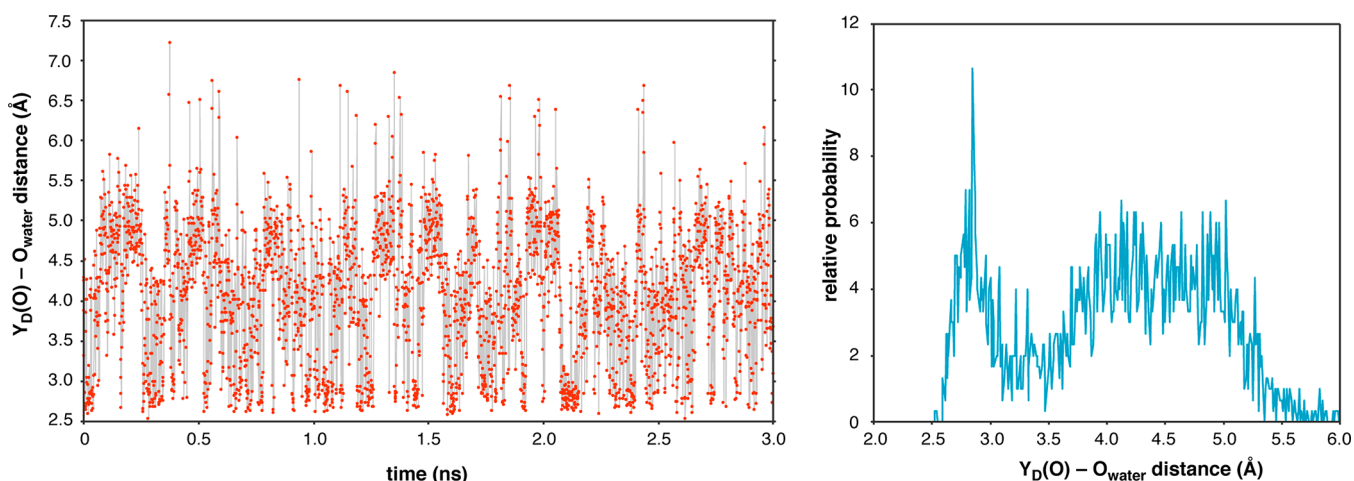
Figure 4. Results of MD calculations regarding the evolution of $Y_D(O)-O_{water}$ distances and their probability distribution from a 3 ns production run.

N_π) site of His189 is blocked by hydrogen bonding with the $N_\varepsilon H$ group of Arg294, which acts as a proton donor. As a result, the N_ε (or N_τ) site of the imidazole is protonated and acts as hydrogen bond donor to the phenolic oxygen of the Y_D, while the phenolic proton of Y_D points toward the cavity. Of the two models, one corresponds to the proximal ($\mathbf{1_R}$) and the other to the distal water position ($\mathbf{2_R}$). In model $\mathbf{1_R}$ the proximal water is stabilized by hydrogen bonds with Y_D-OH and the backbone carbonyl of Phe169. In model $\mathbf{2_R}$ the water in the distal position also interacts with the backbone carbonyl but forms a hydrogen bond with Arg180. The distances between $Y_D(O)$ and O_{water} are 2.78 and 4.35 Å for the two optimized models. Importantly, the distal water position is computed to be more stable than the proximal by 4.4 kcal mol^{-1} with the PBE functional. This value is similar to different hybrid functionals and with the larger basis set, i.e., 5.0 kcal mol^{-1} (B3LYP) and 4.6 kcal mol^{-1} (TPSSh). Apparently, the water is better stabilized at the distal position because the interaction with Arg180 is stronger than the interaction with Y_D-OH.

Additional protonation states and hydrogen-bonding patterns have been considered. Model $\mathbf{3_R}$ mimics the hydrogen-bonding pattern of the Y_Z site, with Y_D-OH acting as hydrogen bond donor to the His189. In this case the only stable distribution of protons among Arg294−His189−Tyr160 is that depicted in Figure 3 for model $\mathbf{3_R}$; that is, the imidazole N_δ is protonated and an unusual protonation state of Arg294 is obtained, with its deprotonated N_ε acting as acceptor for the N_δ-H of His189. Note that the total number of protons in model $\mathbf{3_R}$ is reduced by one compared to $\mathbf{1_R}$ and $\mathbf{2_R}$; therefore $\mathbf{3_R}$ is not an isomer of the other two models and their relative energies cannot be compared. A most important result regarding this protonation arrangement is that no optimized structure associated with the proximal water position could be located. Only the distal position of the water molecule gives rise to a stable minimum, with an optimized $Y_D(O)-O_{water}$ distance of 4.25 Å. This is a crucial observation because it implies that under a protonation and hydrogen-bonding scenario directly analogous to that of Y_Z the cavity water *cannot* function as a hydrogen bond partner to Y_D, and as will be discussed below, this excludes a role of water in Y_D oxidation. By contrast, the protonation state of models $\mathbf{1_R}$

and $\mathbf{2_R}$ naturally gives rise to two minima and hence to the dual occupancy of the water molecule.

In terms of energetics, the results based on the protonation scheme of models $\mathbf{1_R}$ and $\mathbf{2_R}$ are consistent with the observations from crystallography discussed above, which indicate that the distal position should be more stable. However, our results are in contrast to the computed values reported by Saito et al.,[50] who suggested that the proximal position is instead more stable than the distal position by a similar energy margin of ca. 4 kcal mol^{-1}. After close inspection of the computational models and methods used by Saito et al., we conclude that the reason for this large discrepancy on the order of 10 kcal mol^{-1} is the very limited QM region employed in that QM/MM study, which likely leads to artifacts in the evaluation of hydrogen bonds. It appears that some parts of the model, despite being in hydrogen-bonding interaction with the cavity water, were not included in the QM region but treated with force-field parameters. Since the water molecule and the different hydrogen-bonding partners available in the cavity were not uniformly part of the same theoretical representation, their interactions were not treated with a common level and type of theory. The definition of the computational model and the unequal representation likely explains why the reported relative energetics in the study of Saito et al. deviate from those reported here. In the present work all hydrogen-bonding interactions are treated equally at a fully quantum mechanical level with large converged basis sets, and hence we suggest that the present values can be considered to be a qualitatively correct representation of the relative stabilities of the two water sites, even if the absolute numerical values may still be open to refinement.

Molecular Dynamics Simulations of Cavity Water Distribution. To further evaluate this assignment using a methodologically orthogonal approach, we performed molecular dynamics simulations on a complete PSII monomer. Along the trajectory of the MD simulation we observed that the water molecule explores the whole cavity. However, from the analysis of the results it is clear that two regions are most frequently visited on average, and these correlate directly with the proximal and distal sites discussed above. The proximal site in the MD simulations is more well-defined, having a rather sharp peak at ca. 2.75 Å in the graph depicting the time evolution of the distance between the O atom of the cavity

water and the phenolic oxygen of Y_D. In contrast, there is no well-defined unique minimum that can be ascribed to the distal site, but rather a broad distance range at ca. 4.0–5.0 Å. This encompasses the range of "distal" water positions reported in various crystal structures (see Table 1), a fact that supports the validity of the simulations and at the same time justifies the spread of crystallographic values.

The difference between the two sites relates to the fact that the proximal position is spatially more restricted, and when the water occupies this position, there is one optimal hydrogen-bonding arrangement, which coincides with that of the QM model shown in Figure 2. On the other hand, there is greater conformational flexibility in the distal region as a combined result of the larger space and the flexibility of the Arg180 side chain. In fact, we observed that water may exit and re-enter the cavity (points with $Y_D(O)-O_{water}$ distances longer than those that fall within the distal range in Figure 4), a motion facilitated by tilting of the Arg180 guanidinium group. What is most relevant for the preceding discussion is the distribution of the cavity water among the proximal and distal positions. In this respect the MD simulations show that the distal region is more frequently occupied by the cavity water molecule. This is also the region to which water tends to drift toward in MD runs initiated with water at the proximal position (see Supporting Information Figure S1 for an additional MD simulation that demonstrates this point). Using the distance of 3.5 Å as a cutoff point between proximal and distal regions, the frames with $Y_D(O)-O_{water}$ distances shorter than 3.5 Å account for ca. 26.6% of the population, while those above 3.5 Å account for 73.4%. Discounting the frames where water is outside the cavity and using the distance of 5.5 Å as a second cutoff for the distal region, the relative populations become 27.3% and 72.7%, respectively.

In conclusion, both classical MM/MD simulations on a PSII monomer and quantum chemical optimizations with large QM cluster models support that in the reduced state of Y_D the cavity water occupies preferentially the distal position, although access to the less favorable proximal position is not energetically inhibited.

Formation of the Tyrosyl Radical. Based on the protonation state of the residues discussed above, His189 cannot function as a proton acceptor unless the entire protonation state of the His189–Arg294 pair is altered so that His189 becomes a hydrogen bond acceptor in its interaction with Y_D. Interestingly, Arg294 was identified by targeted random mutagenesis studies as functionally important for PSII.[115] With the models favoring the orientation of the phenolic proton of the tyrosine toward the cavity it can be concluded that the cavity water is the most likely recipient of the proton upon oxidation of Y_D. By attempting to oxidize the models shown in Figure 3, it becomes apparent that model 2_R, which contains the water at the distal position, cannot be oxidized: upon electron removal from the model, we observed no coupled deprotonation of Y_D and no spin localization. Rather, the unpaired spin density was sparsely distributed over the model (see Figure S2). This result appears to be independent of the density functional used (e.g., PBE0,[116,117] B3LYP,[99] TPSS0,[118] and TPSSh[100]). This particular observation emphasizes that Y_D cannot be oxidized with distal occupancy of the water molecule when His189 is a hydrogen bond donor to Y_D. By contrast, oxidation of model 1_R with the water at the proximal position proceeds easily and yields a tyrosyl radical with concomitant shift of the phenolic proton to

the proximal water (model 1_{Ox} of Figure 5). The optimized geometry contains the tyrosyl radical bound with two
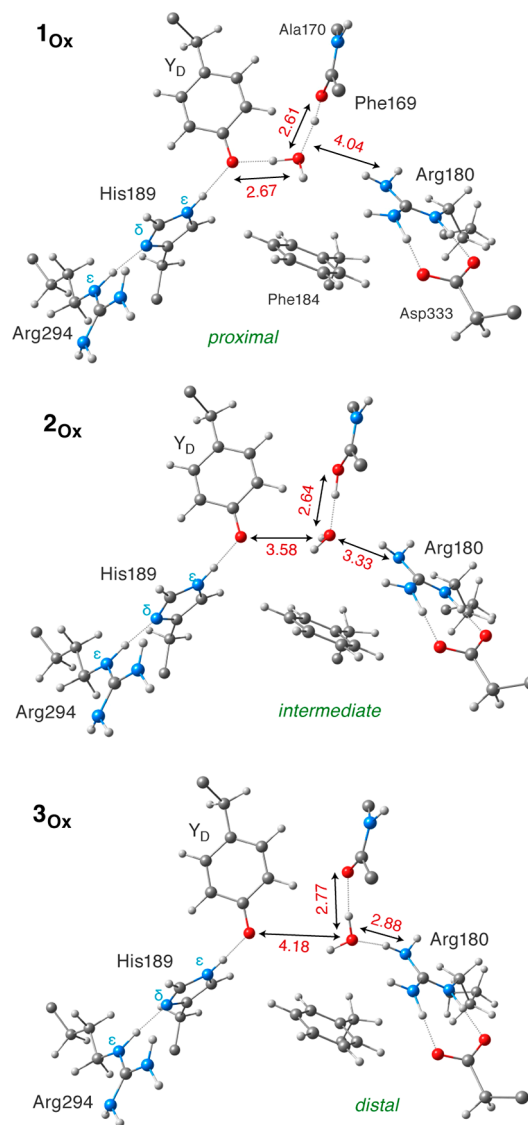

Figure 5. Parts of optimized models with oxidized $Y_D^{\bullet}$ depicting different positions of the cavity water with respect to the translocation of the phenolic proton. Selected distances are indicated (in Å) between the O atom of the cavity water, the O atom of Y_D, the O atom of the Phe169 peptide carbonyl, and the N_η atom of Arg180. When the proton is still present in the cavity, the cavity water is stabilized in either the proximal (1_{Ox}) or an intermediate position (2_{Ox}). Model 3_{Ox} can be seen as either a model related to the other two, where the proton has left the cavity and the water is stabilized exclusively in the distal position, or as the oxidized form of model 3_R, where oxidation of Y_D is accompanied by proton shift to His189–Arg294 and the water, at the distal position regardless of the oxidation state of Y_D, has no involvement.

hydrogen bonds, from His189 and the proximal water. As a result of the strong hydrogen-bonding interaction between the proximal water–Y_D pair, the hydrogen-bonding distance involving the Y_D–His189 pair becomes larger (O···N = 3.03 Å). Following the deprotonation of the Y_D–OH, we observed no explicit formation of a hydronium ion (H_3O^+), but rather a proton shift toward the peptide carbonyl of Phe169 (see Figure 5).

Table 2. Computed g Values and O Löwdin Spin Population for the $Y_D^\bullet$ Models, Compared to the Experimental Ranges of Values Reported under Various Conditions

model	g_x	g_y	g_z	ρ_O
1_{Ox}	2.0063	2.0044	2.0022	0.325
2_{Ox}	2.0073	2.0044	2.0021	0.347
3_{Ox}	2.0073	2.0043	2.0021	0.345
experiment[a]	2.0074−2.0078 or 2.0064[b]	2.0042−2.0045	2.0020−2.0023	0.28[119,120]

[a]Detailed experimental g values from available EPR studies are listed in Table S2. [b]g_x value from tyrosyl radical generated at 1.8 K at pH ca. 8.5.[47]

In model 2_{Ox} the water is optimized in a position that is intermediate between proximal and distal ($Y_D(O)-O_{Water}$ = 3.58 Å) with the proton essentially attached to the backbone carbonyl of Phe169. Models 1_{Ox} and 2_{Ox} are distinct geometric minima, but they are not energetically distinguishable by DFT because the relative energy difference between the models is 0.0 or 0.3 kcal mol^{-1} with the B3LYP and TPSSh functionals, respectively, although 1_{Ox} is 3.2 kcal mol^{-1} lower than 2_{Ox} with the PBE functional. We note that structures 1_{Ox} and 2_{Ox} have not been previously identified in the literature. The third model shown in Figure 5 is 3_{Ox}, with $Y_D(O)\cdots O_{Water}$ = 4.18 Å, i.e., with water at the distal position. This can be viewed in two ways: (1) as directly related to the other two models in a hypothetical sequence $1_{Ox} \rightarrow 2_{Ox} \rightarrow [3_{Ox} + H^+]$, where the cavity water takes the proton at the proximal position (1_{Ox}), moves to the intermediate position (2_{Ox}), and then is stabilized at the distal position with the proton having left the cavity; or (2) as the oxidized form of model 3_R in which a proton translocation has taken place from Y_D to His189-N_ε and from His189-N_δ to Arg294.

Our calculations suggest that a hydronium cation cannot be stabilized at the distal position. Additionally, no Y_D-oxidized model with an overall proton configuration similar to 3_{Ox} could be obtained with the water at the proximal position. These results admit two interpretations. First, if 3_R better reflects the reduced state of Y_D, then oxidation follows a "Y_Z"-like proton shift; that is, His189 is the immediate proton acceptor. In this scenario the water is exclusively stabilized at a unique minimum in the distal position and hence is only a spectator, playing no role in the oxidation and deprotonation of Y_D. The obvious problem with this interpretation is that it does not allow for occupation of the proximal position under *any* redox state of Y_D. If, on the other hand, the pair $1_R/2_R$ better reflects the reduced state of Y_D, then upon oxidation, the proton either remains within the cavity as a hydronium at proximal or intermediate positions (1_{Ox} and 2_{Ox}) or leaves the cavity and the water is stabilized in the distal position (3_{Ox}). This accommodates the existence of distinct minima for the water position and implicates the cavity water directly in Y_D oxidation and the release of the phenolic proton. The precise mechanism of proton removal in the latter scenario cannot be directly deduced from the QM models described here, but it would likely involve participation of Arg180 as proposed by Saito et al.[50]

EPR Spectroscopy: g-Tensors. In an attempt to identify connections between the three models presented above and the available EPR observations, we examine the g-tensors of the three oxidized models. The computed g values of all models are tabulated in Table 2 and compared with the experimental values. The orientation of principal g-matrix components is shown in Figure 6.

The g values of phenoxyl radicals depend on two factors, which are in turn influenced by the protein environment (local
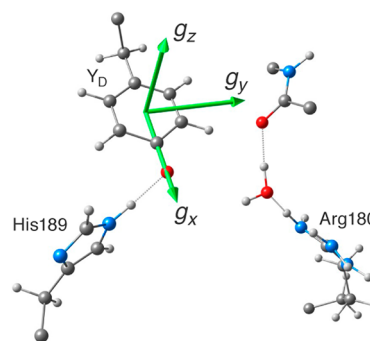

Figure 6. Orientation of the principal g-matrix components for the $Y_D^\bullet$ radical (model 3_{Ox} is used for this plot).

electrostatics) and hydrogen bonding: (1) the unpaired spin density on the oxygen atom, which has the largest spin−orbit coupling constant, and (2) the relative energy difference between the oxygen-based p_z and p_y orbitals. The p_z orbital of the oxygen atom is orthogonal to the ring plane and contributes to the SOMO of the radical. The g_x value is affected by the energy difference between the SOMO and the in-plane p_y lone pair of the phenolic oxygen. The relative energy of the in-plane p_y orbital with respect to the SOMO is influenced by the number, strength, and orientation of hydrogen bonds to the oxygen atom. In-plane hydrogen bonds (from D2-His189 in the case of Y_D) stabilize the p_y orbitals, increasing the energy difference between the p_y and the SOMO, which results in less effective spin−orbit coupling and decreased g_x values.

Shifts in g values as a response to the number and orientation of hydrogen bonds to tyrosine radicals have been studied for simple models[121−124] as well as explicitly for the $Y_Z^\bullet$ of PSII[102] and the $Y_{731}^\bullet$ of ribonucleotide reductase (RNR).[125,126] In the case of $Y_Z^\bullet$ the g_x value was shown to decrease with the number of hydrogen bonds, and this change tracked also the decrease in oxygen spin population.[102] For example, the associated g_x values of $Y_Z^\bullet$ with the one, two, and three hydrogen bonds were reported to be 2.0072, 2.0063, and 2.0054, respectively. It was also demonstrated that the g_x value for any specific hydrogen-bonding scenario depends on the $Y_Z(O)\cdots H$ distance that affects the unpaired spin density on the oxygen, the atom with the largest spin−orbit coupling. Elaborate studies conducted on the redox-active NH_2Y_{730} radical[126] of RNR yielded a g_x value of 2.0052 as characteristic of three hydrogen bonds associated with the radical. The above observations clearly delineate the direct correlation between the number of hydrogen bonds and the g_x values of the phenoxyl radical.

This analysis is fully consistent with the present results for the Y_D models. Specifically, models 2_{Ox} and 3_{Ox} have similar g_x values (2.0073), as both contain only one hydrogen bond to the tyrosyl radical, from the N_ε (N_τ) of His189. By contrast, in

model 1_{Ox} the g_x value decreases to 2.0063 as a result of the two hydrogen bonds, i.e., from His189 and from the proximal water/hydronium. Only the g_x value differs between the three models, while g_y and g_z remain the same. Therefore, the difference in g_x is directly correlated to the number of hydrogen bonds and therefore to the position of the cavity water. Even though the intermediate and distal water positions cannot be distinguished because the $Y_D^\bullet$ radical in both cases appears with the same g_x of 2.0073, the present results enable us to conclusively and uniquely correlate the occupation of the proximal water position with the g_x value of 2.0063.

It has been observed experimentally that a $g_x \approx 2.0064$ signal is obtained when Y_D is oxidized under high pH conditions at cryogenic temperatures.[46,47,72] Importantly, upon increasing the temperature, the g_x shifts to 2.0075−2.0078. As will be discussed in the following, this change in the g_x value does not reflect the protonation state of His189, as assumed in past literature,[47,127] but is correlated with the movement of the proton-accepting water inside the cavity.

EPR Spectroscopy: Hyperfine Coupling Constants. In addition to the g-tensor, an important parameter that can offer insight into the electronic structure of the tyrosyl radical and help in evaluating computational models is the hyperfine coupling constants (HFC) for protons and heavier nuclei bound to or strongly interacting with it.[71,105,119,120,122,127−137] In addition to proton HFCs, Brynda and Britt have analyzed the ^{13}C and ^{15}N HFCs using a computational Tyr−His model,[122] and we refer the interested reader to that work for a discussion of the data. Here we will briefly focus on selected data relating only to the protons/deuterons because they are most relevant to the subject of microsolvation of $Y_D^\bullet$. Two types of ^2H ENDOR HFCs have been reported, i.e., where the tyrosyl radical is generated under physiological pH (6.5)[79] and high pH (8.7)[46] conditions. Radicals generated under both conditions give the characteristic $g_x \approx 2.0074$ signal,[71] which implies that $Y_D^\bullet$ interacts only with His189; that is, N_ε (N_τ) acts as the sole hydrogen bond donor to $Y_D^\bullet$.[131] The experimentally fitted HFC parameters for both cases are similar (Table 3), suggesting that the pH difference does not change the immediate protonation environment of $Y_D^\bullet$ under physiological temperatures. The computed HFCs for the His189 N_ε deuteron for models that correspond to the same class of g_x signal, i.e., for models 2_{Ox} and 3_{Ox}, agree well with the experimental values (Table 3), which again confirms that the radical is bound with only one hydrogen bond, to His189.

Table 3. Computed Hyperfine and Quadrupole Tensor Components (MHz) for Exchangeable Deuterons

model	H-bond partner	A_x	A_y	A_z	Q_x	Q_y	Q_z
1_{Ox}	His$_{189}$-N$_\varepsilon$D	1.01	−0.60	−0.47	0.110	−0.062	−0.048
	^2D_2O	1.29	−0.86	−0.77	0.078	−0.049	−0.029
2_{Ox}	His$_{189}$-N$_\varepsilon$D	1.35	−0.82	−0.73	0.096	−0.055	−0.041
3_{Ox}	His$_{189}$-N$_\varepsilon$D	1.34	−0.79	−0.71	0.096	−0.055	−0.041
expt (pH 6.5)[79]		1.10	−0.59	−0.51	0.300	−0.190	−0.110
expt (pH 8.7, relaxed)[46]		1.06	−0.58	−0.48	0.11	−0.07	−0.04
expt (pH 8.7, unrelaxed),[46a]		1.59	−0.91	−0.68	0.14	−0.074	−0.066

[a]Unrelaxed $Y_D^\bullet$ intermediate trapped at 7 K. The uncertainty in the calculated parameters is estimated to be 20%.[125,126] The components of the A and Q tensors are described such as $|x| > |y| > |z|$.

Similar agreement is obtained with the computed HFCs for the protons of the tyrosyl ring, ^{13}C (Y_D) and ^{17}O (Y_D) (Figure S3 and Tables S3−S7), which also agree well with experimental data,[71,119,120,132] support the orientation and environment of the Y_D radical in the present models. The computed quadrupole tensors provided in Table 3 agree somewhat better with the results obtained under high pH conditions, but at this point we are running the risk of overinterpreting both our results and the information content of the experiment. The experimentally fitted distance between the tyrosyl oxygen and the His189-bound proton was reported as 1.84 and 1.75 Å at physiological and high pH, respectively. These are consistent with the computed distances (1.79 and 1.78 Å for models 2_{Ox} and 3_{Ox}), but the calculations clearly suggest that the fitted parameters derived from experimental data independently of explicit atomistic models would be worth revisiting using QM-optimized distances and accounting for the cavity water. Overall, the agreement of the computed HFCs for the His189 proton with the experimental values is consistent with the structural interpretation derived from the g values.

As discussed above, the $Y_D^\bullet$ radical generated at 1.8 K and pH 8.5 shows a $g_x = 2.0064$, which we assigned to a structural configuration with a proximal water-like model 1_{Ox}. Table 3 also reports computed HFCs for model 1_{Ox}, in which $Y_D^\bullet$ interacts directly with two hydrogens, the N_ε-H of His189 and the proximal water molecule. The HFC parameters for 1_{Ox} suggest comparable HFCs for the two partners. Interestingly, the computed parameters for the proximal water resemble closely those of the His189 hydrogen in the other two models (2_{Ox} and 3_{Ox}), whereas the His189 hydrogen in 1_{Ox} experiences relatively weaker coupling. Both values can be considered consistent with experimental HFCs of higher-g_x species, but comparisons with the cryogenic HFCs are not entirely reliable for two reasons. First, no spectral simulations have been reported with the assumption of the Y_D radical interacting with more than one deuteron.[46] Second, based on the g value calculations, model 1_{Ox} is only an approximate structural model for Y_D oxidation at cryogenic temperature and high pH, but cannot be an exact representation of the cryogenic state because the positions of heavy atoms are optimized. In our view it is not possible to either deduce from experiment the extent of proton shift toward the proximal water or to model reliably with standard QM models the evolution of proton movement along the Y_D−O···H···OH$_2$···OC(Phe169) network at the initial stages of Y_D oxidation. Nevertheless, the present results strongly suggest that existing studies should be revisited and the data refitted with the acknowledgment that the cryogenic state involves two coupled deuterons.

Computed HFCs of heavier nuclei (^{13}C, ^{15}N, and ^{17}O) are reported in the Supporting Information and compared with the available experimental data (Table S7). We find that the models 2_{Ox} and 3_{Ox} show excellent agreement with the experimental ^{13}C and ^{17}O HFC values.[119] This is important because the experimental g_x value of the isotopically labeled Y_D radical was found to be 2.0076, which is consistent with the g_x values computed for the same models, i.e., with the Y_D radical bound with only one hydrogen bond to His189. Another result that corroborates this observation is the isotropic hyperfine coupling for the ^{15}N (N_ε of His189). While for model 1_{Ox} a rather low value of 0.26 MHz was computed, for models 2_{Ox} and 3_{Ox} the computed values are 0.49 and 0.58 MHz, respectively, which agree well with the ^{15}N ENDOR

determined value of 0.8 MHz.[131] This reaffirms the conclusions of the experimental report that the His189 is the direct, and only, hydrogen-bonding partner of the Y_D radical.

■ DISCUSSION

In the reduced state of Y_D, the cavity water molecule can occupy two positions in the cavity defined by the cluster of phenylalanine residues shown in Figure 2, proximal and distal with respect to the Y_D residue (Figure 3). In both positions the backbone carbonyl of Phe169 plays the role of H-bond acceptor; in the proximal position the water is additionally stabilized by a H-bond to Y_D, which therefore acts as proton donor (model 1_R), while in the distal (models 2_R and 3_R) it is stabilized by an additional H-bond to Arg180. The results presented above show that the distal position is energetically preferred compared to the proximal position when Y_D is reduced. This conclusion is in contrast with a previous suggestion,[50] but it is in line with available crystallographic data and supported both by large-scale QM calculations and by MD simulations. Our models additionally suggest a correlation between the protonation pattern in the Arg294−His189−Y_D triad and the water position: if Y_D acts as a proton donor to His189, then the cavity water cannot be stabilized in the proximal position.

Two ideas can be formulated regarding the deprotonation of Y_D upon oxidation: deprotonation to His189[17,44−48,72] or to the cavity water molecule.[50,51,53−55] The idea of Y_D deprotonation to the His189 parallels the mechanism proposed for the other redox-active Y_Z residue, which deprotonates to the coupled His190. The computational models presented here can in principle accommodate the scenario of a Y_Z-like proton shift, which is equivalent to model 3_R being oxidized to model 3_{Ox}. In the following we will discuss why the latter scenario is disfavored and how the computed energetics of water distribution and the related EPR parameters explain the whole range of EPR observations, including the temperature dependence of EPR spectra, on the basis of the oxidized models presented here. Simultaneously, compelling evidence in favor of the present models and of water-assisted oxidation and deprotonation comes from the structural explanation of the biphasic kinetics of Y_D oxidation.

Water Distribution and Kinetics of Y_D Oxidation. The two results—(a) that the distal water position is more stable than the proximal when Y_D is reduced and (b) that Y_D can be oxidized only when water is found in the proximal position—imply that oxidation of Y_D for the *majority* of PSII centers would be inhibited because of the requirement for distal water to move to the less favorable proximal local minimum. This provides a natural explanation for a wide range of experimental observations. It is known that no Y_D centers undergo oxidation at cryogenic temperature (5 K, at pH 6.5).[25] According to the present models, under such conditions almost all Y_D centers are expected to be associated with the distal water and the movement of water to the proximal position is expected to be blocked. This dependence of Y_D oxidation on the spatial availability of the cavity water as proton acceptor fundamentally differentiates the oxidation characteristics of Y_D from the Y_Z radical of PSII. It is also in line with the distinct rates of oxidation for Y_D and Y_Z: under physiological conditions (pH ≈ 6.5), Y_D is oxidized on the microsecond time scale ($t_{1/2}$ > 150 μs), much slower compared to Y_Z ($t_{1/2}$ ≈ 2−10 μs).[22]

Mamedov and co-workers studied the oxidation kinetics of Y_D at different pH values and concluded that at pH 4.7 and 6.3

the oxidation kinetics of Y_D are biphasic; that is, they exhibit a fast and a slow phase.[53,54] Crucially, it was observed that the amplitude of the slow phase is always higher than that of the fast phase. The hypothesis that the two phases may correlate with the position of the cavity water is fully borne out by the detailed computational models presented here. The observation of the dominance of the slow phase is consistent with the result that the majority of Y_D centers have the cavity water present at the distal position, whereas the proximal position is occupied only in a minority of centers and gives rise to the small-amplitude fast phase in oxidation kinetics. Therefore, our computational models fully agree with the suggested correlation of oxidation kinetics and water distribution proposed for the low-pH situation in the studies by Ahmadova et al.[53] and Sjöholm et al.[54] (but not for the high-pH situation as will be discussed in the following).

Experiments performed with the presence of DCMU (3-(3,4-dichlorophenyl)-1,1-dimethylurea), an inhibitor of the Q_B site that blocks forward electron transfer in PSII, forcing $Q_A^-S_2$ recombination, show only the fast phase irrespective of the pH of the sample.[53] This study concluded that the fast-phase Y_D oxidation outcompetes the $Q_A^- S_2$ recombination, whereas the rate of the slow-phase oxidation (according to the present interpretation, Y_D centers with distal water) lags compared to the $Q_A^- S_2$ recombination. This is why the slow phase is not observed. This analogy is evident from the fact that the amplitude of the fast phase is the same with or without DCMU. In addition, only 24% Y_D centers get oxidized at pH 6.3 with DCMU compared to 63% at the same pH without DCMU. The above results become transparent in terms of their structural interpretation in view of the present models that support simultaneously the enhanced stability of the distal water position and the necessity of a proximal water for Y_D oxidation.

Structural Explanation of EPR Spectroscopy. Compelling evidence for correlating experimental observations with the water position comes from comparing EPR data with the computed g-matrix values we report for our models. Two types of EPR signal can be distinguished based on the g_x value of the Y_D radical, close to either 2.0064 or 2.0075. Y_D exhibits interesting EPR properties under high pH conditions.[22,25,46,47,72] Faller et al. showed that at high pH the reduced Y_D can be oxidized even at 1.8 K, giving rise to an EPR signal with a g_x of 2.0064.[47,72] Upon increasing the temperature (77 K), the increased g_x value of 2.0075 was observed.[47] HF-EPR experiments by Chatterjee et al.[46] are consistent with these observations: an unrelaxed state could be trapped at 7 K upon Y_D oxidation with a g_x value of 2.0067, while upon thermal relaxation, the g_x value increases to 2.0078. The g_x value of 2.0074−2.0078 is observed experimentally for the Y_D radical generated under physiological temperatures at any pH value.

The original structural explanation of the two signals implicated proton transfer from Y_D to the N_τ of a singly protonated (at N_π) His189 and formation of a cationic His189 species (low g_x), which deprotonates (from N_π) at higher temperature, relaxing to the lower-field signal.[47] The present calculations do not support this scenario. Instead, the "cryogenic" signal corresponds directly to the value computed for model 1_{Ox} (g_x = 2.0063), and hence we attribute this to the presence of two hydrogen bonds to Y_D or, equivalently, to the presence of water (as proton acceptor) at the proximal position. According to this interpretation, the experimentally

observed change in g_x is not related to the behavior of the histidine, but to the movement of the water/hydronium from the proximal position (model $\mathbf{1_{Ox}}$) to an intermediate position with the proton retained in the cavity (model $\mathbf{2_{Ox}}$) or a distal position with the proton removed from the cavity (model $\mathbf{3_{Ox}}$). Both $\mathbf{2_{Ox}}$ and $\mathbf{3_{Ox}}$ have g_x values of 2.0073 and are consistent with the EPR of a tyrosyl radical having only *one* hydrogen bond (to His189). Therefore, this signal implies that the water has moved away from the proximal position after accepting the proton. However, the existing data do not allow us to determine whether the proton has left the cavity (model $\mathbf{3_{Ox}}$) or not (model $\mathbf{2_{Ox}}$).

pH Dependence of Y_D Oxidation. As already stated above, the pH affects the oxidation of Y_D. We suggest that the molecular basis of this effect relates to the change in the relative stability of the proximal and distal water positions. Y_D is known to outcompete Y_Z in high-pH conditions; for example at pH 8.5 oxidation of Y_D becomes extremely fast ($t_{1/2} \approx 190$ ns),[22] and recent results from Schlodder et al. report this rate to be even faster ($t_{1/2} \approx 30$ ns) at pH 9.[138] These faster oxidation rates also depend on the location of the cation on the reaction center, and it is suggested[22,138] that in high-pH (8.5) conditions the major proportion of cation resides on the P_{D2} side of the reaction center,[138,139] unlike in low-pH conditions, where the cation is mainly localized on the P_{D1} side.[30] This charge shift presumably makes electron transfer faster from the reduced Y_D to P_{680} ($t_{1/2} \approx 30-190$ ns). Ahmadova et al.[53] observed nearly 78% of the fully oxidized Y_D centers at pH 8.5. At pH 8.5 it is observed that the Y_D oxidation follows a single-exponential phase with fast oxidation rates.[53] This was attributed to the deprotonation of Y_D in the reduced form (i.e., a tyrosinate anion), which would render the subsequent oxidation a pure electron transfer event.[53] Our computational models however provide no support for this for two reasons: first, the identification of a minimum with a Y_D-O⁻ form was not possible, and second, the radical formed upon oxidation of this hypothetical deprotonated form would be inconsistent with the low g_x value observed in EPR and assigned to model $\mathbf{1_{Ox}}$. Therefore, we suggest that the observed effects are not attributable to changes in protonation state of the reduced Y_D residue,[50,53,54] but are again associated with the distribution of water within the cavity. Specifically, the observations at high pH would be consistent with association of most Y_D centers with the proximal water. According to the model presented in the present work, the observations may reflect a shift in the relative energetics of proximal vs distal water positions, that is, a progressive stabilization of the proximal position at increasing pH values.

It is acknowledged that the present models and computational approaches cannot provide a detailed view of how protonation states of residues respond to bulk pH changes or how hydrogen-bonding networks are rearranged at large scales within PSII. Hence, it is also unclear how increasing bulk pH might stabilize the proximal position. However, based on the structure of the cavity we suggest that a possible local explanation of the observed effects is that at high pH the distal water position might be destabilized by perturbation of the Arg180−Asp333 salt bridge that is in contact with the protein surface through a rather short water channel.[51] The result would be the preferential occupation of the proximal water position at high pH, rendering the Y_D readily oxidizable even at cryogenic temperatures since water movement is no longer required to switch on the electron transfer. The special

importance of Arg180 was highlighted in site-directed mutagenesis studies by Manna et al.,[140] who reported that mutations at the Arg180 residue resulted in EPR signals attributed to the Y_D radical being of reduced intensity and altered line shape. More importantly, Arg180 mutants had limited oxygen evolution capacity of PSII, and the amount of enzyme present in thylakoids was reduced, demonstrating the functional importance of this residue for smooth redox behavior at the Y_D site.

Fate of the Proton. The fate of the phenolic proton after oxidation of the Y_D relates to all three factors: the relative stabilities of the cavity water positions, the effect of pH, and the role of the Arg180−Asp333 salt bridge. A detailed scenario on a possible deprotonation pathway has been presented by Ishikita and co-workers,[50,51] who suggested that after Y_D oxidation the proton is transferred toward the bulk via proton exchange through Arg180−Asp333 and a series of water molecules beyond this salt bridge. A recent FTIR study[52] from Nakamura and Noguchi reported the detection of the proton released upon Y_D-OH oxidation to the bulk, assuming a correspondence of their observations with the model of Saito et al. On the other hand, that model required a very large energy for the return of the proton (ca. 80−120 kcal/mol) upon Y_D reduction.

The experimental observations on the deprotonation step remain debatable. A proton inventory study by Barry and co-workers[66] supported the existence of multiple proton donation pathways to the Y_D radical at high pH, one of them involving multiple protons and the other a single proton. The proton-coupled electron transfer (PCET) mechanism under high pH conditions is supported by the difference FTIR study of Heinerwadel et al.,[68] where it is proposed that Y_D remains protonated under a pH range 6.0−10.0 and is involved in a strong hydrogen bond. A pure ET process upon oxidation is instead supported by a recent EPR study of Schlodder et al.,[138] where no change in oxidation rates was observed upon introducing exchangeable protons. In addition, their flash-induced absorbance study reports that Y_D oxidation is independent of temperature between 5 and 250 K at pH 9.

If we focus on the EPR results, a clear conclusion based on the present oxidized models $\mathbf{2_{Ox}}$ and $\mathbf{3_{Ox}}$ is that they correlate equally well with the $g_x \geq 2.0073$ tyrosyl EPR signals and hence accommodate two distinct possibilities equally well: that the proton remains in the cavity ($\mathbf{2_{Ox}}$) or that the proton has left the cavity ($\mathbf{3_{Ox}}$). The latter model reflects the scenario described by Saito et al.[50,51] The former, however, represents a possibility that has not been previously represented by computational models and can be of relevance in interpreting experimental results obtained at different pH values. Beyond the agreement of this "proton-in-the-cavity" $\mathbf{2_{Ox}}$ model with the EPR, it is interesting to note that it would be consistent with one of the proposed roles of the Y_D residue. Specifically, it has been suggested that the oxidized Y_D might be exerting an electrostatic effect on the primary charge separation site, pushing the electron hole toward the P_{D1} side of P_{680} and hence enhancing the Y_Z-P_{680} donation rates.[22,29,138,139,141] For this function it would be required that the proton is retained near the Y_D residue,[29] i.e., like in model $\mathbf{2_{Ox}}$. The oxidized models described here therefore provide a structural basis for discussing several observations and mechanistic possibilities, but further investigations will be required to clarify which one corresponds to the real system and under which conditions.

CONCLUSIONS

In this work we investigated the role of a confined water in regulating the properties of the redox-active tyrosine Y_D of PSII. Static and dynamic calculations showed that in the reduced form of the tyrosine both proximal and distal positions are stable, but the distal position of the cavity water is energetically favored. When we take into account simultaneously the energetics of cavity water distribution in relation to the ability of Y_D to be oxidized and in relation to the EPR data reported under various conditions, our results are consistent with the idea that the histidine partner plays a different role in Y_Z and Y_D. Whereas D1-His190 accepts the proton of oxidized Y_Z and keeps it in immediate availability to be returned to Y_Z when it is reduced by the manganese cluster of the OEC, our models are consistent with assigning the role of Y_D proton acceptor to the cavity water. The proton can remain within the cavity or not; closer integration of computational modeling and experiment will be required to clarify which scenario is most likely under which conditions. Crucially, if His189 acts as a proton donor to Y_D, which can be considered as a "normal" situation due to its expected interaction with Arg294, then Y_D can be oxidized only when the cavity water is at the proximal position to accept the phenolic proton. In combination with the proposed energetics of water distribution in the cavity, this has profound implications for understanding and explaining the experimental observations of biphasic Y_D oxidation kinetics: the predominant slow phase is ascribed to the majority population where water is found at the distal position. The EPR calculations reported here lead to a natural interpretation of the spectroscopic observations, correlating the observed distribution of g_x values with the position of the cavity water, as opposed to the protonation state or structural relaxation of the His189 residue as previously speculated. In addition, our results suggest a new structural rationalization of the observed pH effect. In contrast to a previous hypothesis that attributed the effect of pH to a direct change of the YD protonation state,[50,53,54] we propose that at high pH the relative stabilities of the two water sites are simply inverted, enabling the oxidation of Y_D at cryogenic temperatures. The detailed structure–spectroscopy correlations described in the present work can serve as the basis for revisiting past experiments in light of the role of the cavity water and also for designing future experiments that will further probe the role of microsolvation in regulating the behavior and function of the redox-active tyrosine.

ASSOCIATED CONTENT

Ⓢ Supporting Information

The Supporting Information is available free of charge on the ACS Publications website at DOI: 10.1021/jacs.8b13123.

Figures S1–S3, Tables S1–S7 (PDF)

AUTHOR INFORMATION

Corresponding Author
*dimitrios.pantazis@kofo.mpg.de
ORCID Ⓞ
Abhishek Sirohiwal: 0000-0002-4073-7627
Frank Neese: 0000-0003-4691-0547
Dimitrios A. Pantazis: 0000-0002-2146-9065
Notes
The authors declare no competing financial interest.

REFERENCES

(1) Blankenship, R. E. *Molecular Mechanisms of Photosynthesis*, 2nd ed.; Wiley: Chichester, 2014; p 312.

(2) Messinger, J.; Noguchi, T.; Yano, J. Photosynthetic O_2 Evolution. In *Molecular Solar Fuels*; Wydrzynski, T. J.; Hillier, W., Eds.; The Royal Society of Chemistry: Cambridge, 2012; pp 163–207.

(3) Rutherford, A. W.; Osyczka, A.; Rappaport, F. Back-Reactions, Short-Circuits, Leaks and Other Energy Wasteful Reactions in Biological Electron Transfer: Redox Tuning to Survive Life in O_2. *FEBS Lett.* **2012**, *586*, 603–616.

(4) Styring, S.; Sjöholm, J.; Mamedov, F. Two Tyrosines that Changed the World: Interfacing the Oxidizing Power of Photochemistry to Water Splitting in Photosystem II. *Biochim. Biophys. Acta, Bioenerg.* **2012**, *1817*, 76–87.

(5) Diner, B. A.; Britt, R. D. The Redox-Active Tyrosines YZ and Y_D. In *Photosystem II*; Springer, 2005; pp 207–233.

(6) Nugent, J. H.; Ball, R. J.; Evans, M. C. Photosynthetic Water Oxidation: The Role of Tyrosine Radicals. *Biochim. Biophys. Acta, Bioenerg.* **2004**, *1655*, 217–221.

(7) Pujols-Ayala, I.; Barry, B. A. Tyrosyl Radicals in Photosystem II. *Biochim. Biophys. Acta, Bioenerg.* **2004**, *1655*, 205–216.

(8) Umena, Y.; Kawakami, K.; Shen, J.-R.; Kamiya, N. Crystal Structure of the Oxygen-Evolving Photosystem II at a Resolution of 1.9 Å. *Nature* **2011**, *473*, 55–60.

(9) Suga, M.; Akita, F.; Hirata, K.; Ueno, G.; Murakami, H.; Nakajima, Y.; Shimizu, T.; Yamashita, K.; Yamamoto, M.; Ago, H.; Shen, J.-R. Native Structure of Photosystem II at 1.95 Å Resolution Viewed by Femtosecond X-ray Pulses. *Nature* **2015**, *517*, 99–103.

(10) Cardona, T.; Sedoud, A.; Cox, N.; Rutherford, A. W. Charge Separation in Photosystem II: A Comparative and Evolutionary Overview. *Biochim. Biophys. Acta, Bioenerg.* **2012**, *1817*, 26–43.

(11) Grabolle, M.; Dau, H. Energetics of Primary and Secondary Electron Transfer in Photosystem II Membrane Particles of Spinach Revisited on Basis of Recombination-Fluorescence Measurements. *Biochim. Biophys. Acta, Bioenerg.* **2005**, *1708*, 209–218.

(12) McEvoy, J. P.; Brudvig, G. W. Water-Splitting Chemistry of Photosystem II. *Chem. Rev.* **2006**, *106*, 4455–4483.

(13) Dau, H.; Zaharieva, I. Principles, Efficiency, and Blueprint Character of Solar-Energy Conversion in Photosynthetic Water Oxidation. *Acc. Chem. Res.* **2009**, *42*, 1861–1870.

(14) Krewald, V.; Retegan, M.; Pantazis, D. A. Principles of Natural Photosynthesis. *Top. Curr. Chem.* **2015**, *371*, 23–48.

(15) Pantazis, D. A. Missing Pieces in the Puzzle of Biological Water Oxidation. *ACS Catal.* **2018**, *8*, 9477–9507.

(16) Vermaas, W. F. J.; Rutherford, A. W.; Hansson, Ö. Site-Directed Mutagenesis in Photosystem II of the Cyanobacterium *Synechocystis sp.* PCC 6803: Donor D is a Tyrosine Residue in the D2 Protein. *Proc. Natl. Acad. Sci. U. S. A.* **1988**, *85*, 8477–8481.

(17) Debus, R. J.; Barry, B. A.; Babcock, G. T.; McIntosh, L. Site-Directed Mutagenesis Identifies a Tyrosine Radical Involved in the Photosynthetic Oxygen-Evolving System. *Proc. Natl. Acad. Sci. U. S. A.* **1988**, *85*, 427–430.

(18) Styring, S.; Rutherford, A. W. In the Oxygen-Evolving Complex of Photosystem II the S_0 State is Oxidized to the S_1 State by D^+ (Signal II_{slow}). *Biochemistry* **1987**, *26*, 2401–2405.

(19) Vass, I.; Styring, S. pH-Dependent Charge Equilibria Between Tyrosine-D and the S States in Photosystem II. Estimation of Relative Midpoint Redox Potentials. *Biochemistry* **1991**, *30*, 830–839.

(20) Vermaas, W. F. J.; Renger, G.; Dohnt, G. The Reduction of the Oxygen-Evolving System in Chloroplasts by Thylakoid Components. *Biochim. Biophys. Acta, Bioenerg.* **1984**, *764*, 194–202.

(21) Messinger, J.; Renger, G. Generation, Oxidation by the Oxidized Form of the Tyrosine of Polypeptide D2, and Possible Electronic Configuration of the Redox States S_0, S_{-1}, and S_{-2} of the Water Oxidase in Isolated Spinach Thylakoids. *Biochemistry* **1993**, *32*, 9379−9386.

(22) Faller, P.; Debus, R. J.; Brettel, K.; Sugiura, M.; Rutherford, A. W.; Boussac, A. Rapid Formation of the Stable Tyrosyl Radical in Photosystem II. *Proc. Natl. Acad. Sci. U. S. A.* **2001**, *98*, 14368−14373.

(23) Ananyev, G. M.; Sakiyan, I.; Diner, B. A.; Dismukes, G. C. A Functional Role for Tyrosine-D in Assembly of the Inorganic Core of the Water Oxidase Complex of Photosystem II and the Kinetics of Water Oxidation. *Biochemistry* **2002**, *41*, 974−980.

(24) Kok, B.; Forbush, B.; McGloin, M. Cooperation of Charges in Photosynthetic O_2 Evolution − I. A Linear Four Step Mechanism. *Photochem. Photobiol.* **1970**, *11*, 457−475.

(25) Havelius, K. G. V.; Styring, S. pH Dependent Competition Between Y_Z and Y_D in Photosystem II Probed by Illumination at 5 K. *Biochemistry* **2007**, *46*, 7865−7874.

(26) Deak, Z.; Vass, I.; Strying, S. Redox Interaction of Tyrosine-D with the S-States of the Water-Oxidizing Complex in Intact and Chloride-Depleted Photosystem II. *Biochim. Biophys. Acta, Bioenerg.* **1994**, *1185*, 65−74.

(27) Feyziyev, Y.; Rotterdam, B. J. v.; Bernát, G.; Styring, S. Electron Transfer from Cytochrome b_{559} and Tyrosine-D to the S_2 and S_3 States of the Water Oxidizing Complex in Photosystem II. *Chem. Phys.* **2003**, *294*, 415−431.

(28) Mamedov, F.; Smith, P. J.; Styring, S.; Pace, R. J. Relaxation Behaviour of the Tyrosine Y_D Radical in Photosystem II: Evidence for Strong Dipolar Interaction with Paramagnetic Centers in the S_1 and S_2 states. *Phys. Chem. Chem. Phys.* **2004**, *6*, 4890−4896.

(29) Rutherford, A. W.; Boussac, A.; Faller, P. The Stable Tyrosyl Radical in Photosystem II: Why D? *Biochim. Biophys. Acta, Bioenerg.* **2004**, *1655*, 222−230.

(30) Saito, K.; Ishida, T.; Sugiura, M.; Kawakami, K.; Umena, Y.; Kamiya, N.; Shen, J.-R.; Ishikita, H. Distribution of the Cationic State over the Chlorophyll Pair of the Photosystem II Reaction Center. *J. Am. Chem. Soc.* **2011**, *133*, 14379−14388.

(31) Diner, B. A.; Bautista, J. A.; Nixon, P. J.; Berthomieu, C.; Hienerwadel, R.; Britt, R. D.; Vermaas, W. F. J.; Chisholm, D. A. Coordination of Proton and Electron Transfer from the Redox-Active Tyrosine, Y_Z, of Photosystem II and Examination of the Electrostatic Influence of Oxidized Tyrosine, $Y_D^\bullet(H^+)$. *Phys. Chem. Chem. Phys.* **2004**, *6*, 4844−4850.

(32) Jeans, C.; Schilstra, M. J.; Ray, N.; Husain, S.; Minagawa, J.; Nugent, J. H. A.; Klug, D. R. Replacement of Tyrosine D with Phenylalanine Affects the Normal Proton Transfer Pathways for the Reduction of P680$^+$ in Oxygen-Evolving Photosystem II Particles from *Chlamydomonas*. *Biochemistry* **2002**, *41*, 15754−15761.

(33) Boussac, A.; Etienne, A. L. Oxido-Reduction Kinetics of Signal II Slow in Tris-Washed Chloroplasts. *Biochem. Biophys. Res. Commun.* **1982**, *109*, 1200−1205.

(34) Debus, R. J. Amino Acid Residues that Modulate the Properties of Tyrosine Y_Z and the Manganese Cluster in the Water Oxidizing Complex of Photosystem II. *Biochim. Biophys. Acta, Bioenerg.* **2001**, *1503*, 164−186.

(35) Dekker, J. P.; Van Gorkom, H. J.; Brok, M.; Ouwehand, L. Optical Characterization of Photosystem II Electron Donors. *Biochim. Biophys. Acta, Bioenerg.* **1984**, *764*, 301−309.

(36) Babcock, G. T.; Blankenship, R. E.; Sauer, K. Reaction Kinetics for Positive Charge Accumulation on the Water Side of Choloplast Photosystem II. *FEBS Lett.* **1976**, *61*, 286−289.

(37) Babcock, G. T.; Sauer, K. A Rapid, Light-Induced Transient in Electron Paramagnetic Resonance Signal II Activated Upon Inhibition of Photosynthetic Oxygen Evolution. *Biochim. Biophys. Acta, Bioenerg.* **1975**, *376*, 315−328.

(38) Saito, K.; Shen, J.-R.; Ishida, T.; Ishikita, H. Short Hydrogen Bond between Redox-Active Tyrosine Y_Z and D1-His190 in the Photosystem II Crystal Structure. *Biochemistry* **2011**, *50*, 9836−9844.

(39) Suga, M.; Akita, F.; Sugahara, M.; Kubo, M.; Nakajima, Y.; Nakane, T.; Yamashita, K.; Umena, Y.; Nakabayashi, M.; Yamane, T.; Nakano, T.; Suzuki, M.; Masuda, T.; Inoue, S.; Kimura, T.; Nomura, T.; Yonekura, S.; Yu, L.-J.; Sakamoto, T.; Motomura, T.; Chen, J.-H.; Kato, Y.; Noguchi, T.; Tono, K.; Joti, Y.; Kameshima, T.; Hatsui, T.; Nango, E.; Tanaka, R.; Naitow, H.; Matsuura, Y.; Yamashita, A.; Yamamoto, M.; Nureki, O.; Yabashi, M.; Ishikawa, T.; Iwata, S.; Shen, J.-R. Light-Induced Structural Changes and the Site of O=O bond Formation in PSII Caught by XFEL. *Nature* **2017**, *543*, 131−135.

(40) Zhang, M.; Bommer, M.; Chatterjee, R.; Hussein, R.; Yano, J.; Dau, H.; Kern, J.; Dobbek, H.; Zouni, A. Structural Insights into the Light-Driven Auto-Assembly Process of the Water-Oxidizing Mn_4CaO_5-Cluster in Photosystem II. *eLife* **2017**, *6*, e26933.

(41) Uto, S.; Kawakami, K.; Umena, Y.; Iwai, M.; Ikeuchi, M.; Shen, J.-R.; Kamiya, N. Mutual Relationships Between Structural and Functional Changes in a PsbM-Deletion Mutant of Photosystem II. *Faraday Discuss.* **2017**, *198*, 107−120.

(42) Koua, F. H. M.; Umena, Y.; Kawakami, K.; Shen, J.-R. Structure of Sr-Substituted Photosystem II at 2.1 Å Resolution and its Implications in the Mechanism of Water Oxidation. *Proc. Natl. Acad. Sci. U. S. A.* **2013**, *110*, 3889−3894.

(43) Young, I. D.; Ibrahim, M.; Chatterjee, R.; Gul, S.; Fuller, F. D.; Koroidov, S.; Brewster, A. S.; Tran, R.; Alonso-Mori, R.; Kroll, T.; Michels-Clark, T.; Laksmono, H.; Sierra, R. G.; Stan, C. A.; Hussein, R.; Zhang, M.; Douthit, L.; Kubin, M.; de Lichtenberg, C.; Vo Pham, L.; Nilsson, H.; Cheah, M. H.; Shevela, D.; Saracini, C.; Bean, M. A.; Seuffert, I.; Sokaras, D.; Weng, T.-C.; Pastor, E.; Weninger, C.; Fransson, T.; Lassalle, L.; Bräuer, P.; Aller, P.; Docker, P. T.; Andi, B.; Orville, A. M.; Glownia, J. M.; Nelson, S.; Sikorski, M.; Zhu, D.; Hunter, M. S.; Lane, T. J.; Aquila, A.; Koglin, J. E.; Robinson, J.; Liang, M.; Boutet, S.; Lyubimov, A. Y.; Uervirojnangkoorn, M.; Moriarty, N. W.; Liebschner, D.; Afonine, P. V.; Waterman, D. G.; Evans, G.; Wernet, P.; Dobbek, H.; Weis, W. I.; Brunger, A. T.; Zwart, P. H.; Adams, P. D.; Zouni, A.; Messinger, J.; Bergmann, U.; Sauter, N. K.; Kern, J.; Yachandra, V. K.; Yano, J. Structure of Photosystem II and Substrate Binding at Room Temperature. *Nature* **2016**, *540*, 453−457.

(44) Tang, X. S.; Chisholm, D. A.; Dismukes, G. C.; Brudvig, G. W.; Diner, B. A. Spectroscopic Evidence from Site-Directed Mutants of *Synechocystis* PCC6803 in Favor of a Close Interaction Between Histidine 189 and Redox-Active Tyrosine 160, Both of Polypeptide D2 of the Photosystem II Reaction Center. *Biochemistry* **1993**, *32*, 13742−13748.

(45) Tommos, C.; Davidsson, L.; Svensson, B.; Madsen, C.; Vermaas, W.; Styring, S. Modified EPR Spectra of the Tyrosine-D Radical in Photosystem II in Site-Directed Mutants of *Synechocystis sp.* PCC 6803: Identification of Side Chains in the Immediate Vicinity of Tyrosine-D on the D2 Protein. *Biochemistry* **1993**, *32*, 5436−5441.

(46) Chatterjee, R.; Coates, C. S.; Milikisiyants, S.; Lee, C.-I.; Wagner, A.; Poluektov, O. G.; Lakshmi, K. V. High-Frequency Electron Nuclear Double-Resonance Spectroscopy Studies of the Mechanism of Proton-Coupled Electron Transfer at the Tyrosine-D Residue of Photosystem II. *Biochemistry* **2013**, *52*, 4781−4790.

(47) Faller, P.; Goussias, C.; Rutherford, A. W.; Un, S. Resolving Intermediates in Biological Proton-Coupled Electron Transfer: A Tyrosyl Radical Prior to Proton Movement. *Proc. Natl. Acad. Sci. U. S. A.* **2003**, *100*, 8732−8735.

(48) Kim, S.; Liang, J.; Barry, B. A. Chemical Complementation Identifies a Proton Acceptor for Redox-Active Tyrosine D in Photosystem II. *Proc. Natl. Acad. Sci. U. S. A.* **1997**, *94*, 14406−14411.

(49) Matsuoka, H.; Shen, J.-R.; Kawamori, A.; Nishiyama, K.; Ohba, Y.; Yamauchi, S. Proton-Coupled Electron-Transfer Processes in Photosystem II Probed by Highly Resolved g-Anisotropy of Redox-Active Tyrosine YZ. *J. Am. Chem. Soc.* **2011**, *133*, 4655−4660.

(50) Saito, K.; Rutherford, A. W.; Ishikita, H. Mechanism of Tyrosine D Oxidation in Photosystem II. *Proc. Natl. Acad. Sci. U. S. A.* **2013**, *110*, 7690−7695.

Journal of the American Chemical Society Article

(51) Saito, K.; Sakashita, N.; Ishikita, H. Energetics of the Proton Transfer Pathway for Tyrosine D in Photosystem II. *Aust. J. Chem.* **2016**, *69*, 991–998.

(52) Nakamura, S.; Noguchi, T. Infrared Detection of a Proton Released from Tyrosine Y_D to the Bulk upon Its Photo-oxidation in Photosystem II. *Biochemistry* **2015**, *54*, 5045–5053.

(53) Ahmadova, N.; Ho, F. M.; Styring, S.; Mamedov, F. Tyrozine D Oxidation and Redox Equilibrium in Photosystem II. *Biochim. Biophys. Acta, Bioenerg.* **2017**, *1858*, 407–417.

(54) Sjöholm, J.; Ho, F.; Ahmadova, N.; Brinkert, K.; Hammarström, L.; Mamedov, F.; Styring, S. The Protonation State Around $Tyr_D/Tyr_D^•$ in Photosystem II is Reflected in its Biphasic Oxidation Kinetics. *Biochim. Biophys. Acta, Bioenerg.* **2017**, *1858*, 147–155.

(55) Sjöholm, J.; Mamedov, F.; Styring, S. Spectroscopic Evidence for a Redox-Controlled Proton Gate at Tyrosine D in Photosystem II. *Biochemistry* **2014**, *53*, 5721–5723.

(56) Migliore, A.; Polizzi, N. F.; Therien, M. J.; Beratan, D. N. Biochemistry and Theory of Proton-Coupled Electron Transfer. *Chem. Rev.* **2014**, *114*, 3381–3465.

(57) Linke, K.; Ho, F. M. Water in Photosystem II: Structural, Functional and Mechanistic Considerations. *Biochim. Biophys. Acta, Bioenerg.* **2014**, *1837*, 14–32.

(58) Takahashi, R.; Sugiura, M.; Noguchi, T. Water Molecules Coupled to the Redox-Active Tyrosine Y_D in Photosystem II as Detected by FTIR Spectroscopy. *Biochemistry* **2007**, *46*, 14245–14249.

(59) Mino, H.; Satoh, J.-i.; Kawamori, A.; Toriyama, K.; Zimmermann, J.-L. Matrix ENDOR of Tyrosine D^+ in Oriented Photosystem II Membranes. *Biochim. Biophys. Acta, Bioenerg.* **1993**, *1144*, 426–433.

(60) Force, D. A.; Randall, D. W.; Britt, R. D.; Tang, X.-S.; Diner, B. A. ^{2}H ESE-ENDOR Study of Hydrogen Bonding to the Tyrosine Radicals $Y_D^•$ and $Y_Z^•$ of Photosystem II. *J. Am. Chem. Soc.* **1995**, *117*, 12643–12644.

(61) Tang, X.-S.; Zheng, M.; Chisholm, D. A.; Dismukes, G. C.; Diner, B. A. Investigation of the Differences in the Local Protein Environments Surrounding Tyrosine Radicals $Y_Z^•$ and $Y_D^•$ in Photosystem II Using Wild-Type and the D2-Tyr160Phe Mutant of *Synechocystis* 6803. *Biochemistry* **1996**, *35*, 1475–1484.

(62) Evelo, R. G.; Hoff, A. J.; Dikanov, S. A.; Tyryshkin, A. M. An ESEEM Study of the Oxidized Electron Donor of Plant Photosystem II: Evidence that $D^•$ is a Neutral Tyrosine Radical. *Chem. Phys. Lett.* **1989**, *161*, 479–484.

(63) Diner, B. A.; Force, D. A.; Randall, D. W.; Britt, R. D. Hydrogen Bonding, Solvent Exchange, and Coupled Proton and Electron Transfer in the Oxidation and Reduction of Redox-Active Tyrosine Y_Z in Mn-Depleted Core Complexes of Photosystem II. *Biochemistry* **1998**, *37*, 17931–17943.

(64) Un, S.; Tang, X.-S.; Diner, B. A. 245 GHz High-Field EPR Study of Tyrosine-D and Tyrosine-Z in Mutants of Photosystem II. *Biochemistry* **1996**, *35*, 679–684.

(65) Hienerwadel, R.; Boussac, A.; Breton, J.; Diner, B. A.; Berthomieu, C. Fourier Transform Infrared Difference Spectroscopy of Photosystem II Tyrosine D Using Site-Directed Mutagenesis and Specific Isotope Labeling. *Biochemistry* **1997**, *36*, 14712–14723.

(66) Jenson, D. L.; Barry, B. A. Proton-Coupled Electron Transfer in Photosystem II: Proton Inventory of a Redox Active Tyrosine. *J. Am. Chem. Soc.* **2009**, *131*, 10567–10573.

(67) Jenson, D. L.; Evans, A.; Barry, B. A. Proton-Coupled Electron Transfer and Tyrosine D of Photosystem II. *J. Phys. Chem. B* **2007**, *111*, 12599–12604.

(68) Hienerwadel, R.; Diner, B. A.; Berthomieu, C. Molecular Origin of the pH Dependence of Tyrosine D Oxidation Kinetics and Radical Stability in Photosystem II. *Biochim. Biophys. Acta, Bioenerg.* **2008**, *1777*, 525–531.

(69) Hienerwadel, R.; Boussac, A.; Breton, J.; Berthomieu, C. Fourier Transform Infrared Difference Study of Tyrosine-D Oxidation and Plastoquinone Q_A Reduction in Photosystem II. *Biochemistry* **1996**, *35*, 15447–15460.

(70) Hienerwadel, R.; Gourion-Arsiquaud, S.; Ballottari, M.; Bassi, R.; Diner, B. A.; Berthomieu, C. Formate Binding Near the Redox-Active TyrosineD in Photosystem II: Consequences on the Properties of TyrD. *Photosynth. Res.* **2005**, *84*, 139–144.

(71) Hofbauer, W.; Zouni, A.; Bittl, R.; Kern, J.; Orth, P.; Lendzian, F.; Fromme, P.; Witt, H. T.; Lubitz, W. Photosystem II Single Crystals Studied by EPR Spectroscopy at 94 GHz: The Tyrosine Radical $Y_D^•$. *Proc. Natl. Acad. Sci. U. S. A.* **2001**, *98*, 6623–6628.

(72) Faller, P.; Rutherford, A. W.; Debus, R. J. Tyrosine D Oxidation at Cryogenic Temperature in Photosystem II. *Biochemistry* **2002**, *41*, 12914–12920.

(73) Un, S.; Atta, M.; Fontecave, M.; Rutherford, A. W. g-Values as a Probe of the Local Protein Environment: High-Field EPR of Tyrosyl Radicals in Ribonucleotide Reductase and Photosystem II. *J. Am. Chem. Soc.* **1995**, *117*, 10713–10719.

(74) Un, S.; Brunel, L.-C.; Brill, T. M.; Zimmermann, J.-L.; Rutherford, A. W. Angular Orientation of the Stable Tyrosyl Radical Within Photosystem II by High-Field 245-GHz Electron Paramagnetic Resonance. *Proc. Natl. Acad. Sci. U. S. A.* **1994**, *91*, 5262–5266.

(75) Hoganson, C. W.; Babcock, G. T. Protein-Tyrosyl Radical Interactions in Photosystem II Studied by Electron Spin Resonance and Electron Nuclear Double Resonance Spectroscopy: Comparison with Ribonucleotide Reductase and in Vitro Tyrosine. *Biochemistry* **1992**, *31*, 11874–11880.

(76) Dorlet, P.; Rutherford, A. W.; Un, S. Orientation of the Tyrosyl D, Pheophytin Anion, and Semiquinone $Q_A^{•-}$ Radicals in Photosystem II Determined by High-Field Electron Paramagnetic Resonance. *Biochemistry* **2000**, *39*, 7826–7834.

(77) Farrar, C. T.; Gerfen, G. J.; Griffin, R. G.; Force, D. A.; Britt, R. D. Electronic Structure of the Y_D Tyrosyl Radical in Photosystem II: A High-Frequency Electron Paramagnetic Resonance Spectroscopic and Density Functional Theoretical Study. *J. Phys. Chem. B* **1997**, *101*, 6634–6641.

(78) Gulin, V. I.; Dikanov, S. A.; Tsvetkov Yu, D.; Evelo, R. G.; Hoff, A. J. Very High Frequency (135 GHz) EPR of the Oxidized Primary Donor of the Photosynthetic Bacteria *Rb. sphaeroides* R-26 and *Rps. viridis* and of Y_D, (signal II) of Plant Photosystem II. *Pure Appl. Chem.* **1992**, *64*, 903–906.

(79) Keßen, S.; Teutloff, C.; Kern, J.; Zouni, A.; Bittl, R. High-Field ^{2}H-Mims-ENDOR Spectroscopy on PSII Single Crystals: Hydrogen Bonding of Y_D. *ChemPhysChem* **2010**, *11*, 1275–1282.

(80) Duan, Y.; Wu, C.; Chowdhury, S.; Lee, M. C.; Xiong, G.; Zhang, W.; Yang, R.; Cieplak, P.; Luo, R.; Lee, T.; Caldwell, J.; Wang, J.; Kollman, P. A Point-Charge Force Field for Molecular Mechanics Simulations of Proteins Based on Condensed-Phase Quantum Mechanical Calculations. *J. Comput. Chem.* **2003**, *24*, 1999–2012.

(81) Jorgensen, W. L.; Chandrasekhar, J.; Madura, J. D.; Impey, R. W.; Klein, M. L. Comparison of Simple Potential Functions for Simulating Liquid Water. *J. Chem. Phys.* **1983**, *79*, 926–935.

(82) Zhang, L.; Silva, D.-A.; Yan, Y.; Huang, X. Force Field Development for Cofactors in the Photosystem II. *J. Comput. Chem.* **2012**, *33*, 1969–1980.

(83) Retegan, M.; Pantazis, D. A. Differences in the Active Site of Water Oxidation among Photosynthetic Organisms. *J. Am. Chem. Soc.* **2017**, *139*, 14340–14343.

(84) Berendsen, H. J. C.; Postma, J. P. M.; van Gunsteren, W. F.; DiNola, A.; Haak, J. R. Molecular Dynamics with Coupling to an External Bath. *J. Chem. Phys.* **1984**, *81*, 3684–3690.

(85) Parrinello, M.; Rahman, A. Polymorphic Transitions in Single Crystals: A New Molecular Dynamics Method. *J. Appl. Phys.* **1981**, *52*, 7182–7190.

(86) Darden, T.; York, D.; Pedersen, L. Particle mesh Ewald: An N·log(N) method for Ewald sums in large systems. *J. Chem. Phys.* **1993**, *98*, 10089–10092.

3229

DOI: 10.1021/jacs.8b13123
J. Am. Chem. Soc. 2019, 141, 3217–3231

(87) Essmann, U.; Perera, L.; Berkowitz, M. L.; Darden, T.; Lee, H.; Pedersen, L. G. A Smooth Particle Mesh Ewald Method. *J. Chem. Phys.* **1995**, *103*, 8577−8593.

(88) Hess, B.; Bekker, H.; Berendsen, H. J. C.; Fraaije, J. G. E. M. LINCS: A Linear Constraint Solver for Molecular Simulations. *J. Comput. Chem.* **1997**, *18*, 1463−1472.

(89) Hess, B.; Kutzner, C.; van der Spoel, D.; Lindahl, E. GROMACS 4: Algorithms for Highly Efficient, Load-Balanced, and Scalable Molecular Simulation. *J. Chem. Theory Comput.* **2008**, *4*, 435−447.

(90) Perdew, J. P.; Burke, K.; Ernzerhof, M. Generalized gradient approximation made simple. *Phys. Rev. Lett.* **1996**, *77*, 3865−3868.

(91) Grimme, S.; Antony, J.; Ehrlich, S.; Krieg, H. A Consistent and Accurate ab initio Parametrization of Density Functional Dispersion Correction (DFT-D) for the 94 Elements H−Pu. *J. Chem. Phys.* **2010**, *132*, 154104.

(92) Grimme, S.; Ehrlich, S.; Goerigk, L. Effect of the Damping Function in Dispersion Corrected Density Functional Theory. *J. Comput. Chem.* **2011**, *32*, 1456−1465.

(93) Weigend, F.; Ahlrichs, R. Balanced Basis Sets of Split Valence, Triple Zeta Valence and Quadruple Zeta Valence Quality for H to Rn: Design and Assessment of Accuracy. *Phys. Chem. Chem. Phys.* **2005**, *7*, 3297−3305.

(94) Sierka, M.; Hogekamp, A.; Ahlrichs, R. Fast Evaluation of the Coulomb Potential for Electron Densities Using Multipole Accelerated Resolution of Identity Approximation. *J. Chem. Phys.* **2003**, *118*, 9136−9148.

(95) Kendall, R. A.; Früchtl, H. A. The Impact of the Resolution of the Identity Approximate Integral Method on Modern ab Initio Algorithm Development. *Theor. Chem. Acc.* **1997**, *97*, 158−163.

(96) Eichkorn, K.; Treutler, O.; Öhm, H.; Häser, M.; Ahlrichs, R. Auxiliary Basis Sets to Approximate Coulomb Potentials. *Chem. Phys. Lett.* **1995**, *240*, 283−290.

(97) Eichkorn, K.; Treutler, O.; Öhm, H.; Häser, M.; Ahlrichs, R. Auxiliary Basis Sets to Approximate Coulomb Potentials (Chem. Phys. Letters 240 (1995) 283−290). *Chem. Phys. Lett.* **1995**, *242*, 652−660.

(98) Cossi, M.; Rega, N.; Scalmani, G.; Barone, V. Energies, structures, and electronic properties of molecules in solution with the C-PCM solvation model. *J. Comput. Chem.* **2003**, *24*, 669−681.

(99) Becke, A. D. Density-Functional Thermochemistry. III. The Role Of Exact Exchange. *J. Chem. Phys.* **1993**, *98*, 5648−5652.

(100) Staroverov, V. N.; Scuseria, G. E.; Tao, J.; Perdew, J. P. Comparative Assessment of a New Nonempirical Density Functional: Molecules and Hydrogen-Bonded Complexes. *J. Chem. Phys.* **2003**, *119*, 12129−12137.

(101) Barone, V. Structure, Magnetic Properties and Reactivities of Open-Shell Species From Density Functional and Self-Consistent Hybrid Methods. In *Recent Advances in Density Functional Methods*; Chong, D. P., Ed.; World Scientific, 1995; Vol. *1*, pp 287−334.

(102) Retegan, M.; Cox, N.; Lubitz, W.; Neese, F.; Pantazis, D. A. The First Tyrosyl Radical Intermediate Formed in the S_2−S_3 Transition of Photosystem II. *Phys. Chem. Chem. Phys.* **2014**, *16*, 11901−11910.

(103) Beal, N. J.; Corry, T. A.; O'Malley, P. J. Comparison between Experimental and Broken Symmetry Density Functional Theory (BS-DFT) Calculated Electron Paramagnetic Resonance (EPR) Parameters of the S_2 State of the Oxygen-Evolving Complex of Photosystem II in Its Native (Calcium) and Strontium-Substituted Form. *J. Phys. Chem. B* **2017**, *121*, 11273−11283.

(104) Kossmann, S.; Kirchner, B.; Neese, F. Performance of modern density functional theory for the prediction of hyperfine structure: meta-GGA and double hybrid functionals. *Mol. Phys.* **2007**, *105*, 2049−2071.

(105) Svistunenko, D. A.; Dunne, J.; Fryer, M.; Nicholls, P.; Reeder, B. J.; Wilson, M. T.; Bigotti, M. G.; Cutruzzolà, F.; Cooper, C. E. Comparative Study of Tyrosine Radicals in Hemoglobin and Myoglobins Treated with Hydrogen Peroxide. *Biophys. J.* **2002**, *83*, 2845−2855.

(106) Bernini, C.; Pogni, R.; Ruiz-Dueñas, F. J.; Martínez, A. T.; Basosi, R.; Sinicropi, A. EPR parameters of amino acid radicals in *P. eryngiiversatile* peroxidase and its W164Y variant computed at the QM/MM level. *Phys. Chem. Chem. Phys.* **2011**, *13*, 5078−5098.

(107) Svistunenko, D. A.; Jones, G. A. Tyrosyl radicals in proteins: a comparison of empirical and density functional calculated EPR parameters. *Phys. Chem. Chem. Phys.* **2009**, *11*, 6600−6613.

(108) Hedegård, E. D.; Kongsted, J.; Sauer, S. P. A. Validating and Analyzing EPR Hyperfine Coupling Constants with Density Functional Theory. *J. Chem. Theory Comput.* **2013**, *9*, 2380−2388.

(109) Neese, F.; Wennmohs, F.; Hansen, A.; Becker, U. Efficient, Approximate and Parallel Hartree−Fock and Hybrid DFT Calculations. A 'Chain-of-Spheres' Algorithm for the Hartree−Fock Exchange. *Chem. Phys.* **2009**, *356*, 98−109.

(110) Neese, F. Prediction of Electron Paramagnetic Resonance g Values Using Coupled Perturbed Hartree−Fock and Kohn−Sham Theory. *J. Chem. Phys.* **2001**, *115*, 11080−11096.

(111) Neese, F. Efficient and Accurate Approximations to the Molecular Spin-Orbit Coupling Operator and Their Use in Molecular g-Tensor Calculations. *J. Chem. Phys.* **2005**, *122*, 034107.

(112) Neese, F. The ORCA Program System. *WIREs Comput. Mol. Sci.* **2012**, *2*, 73−78.

(113) Neese, F. Software Update: the ORCA Program System, Version 4.0. *WIREs Comput. Mol. Sci.* **2018**, *8*, e1327.

(114) Kern, J.; Chatterjee, R.; Young, I. D.; Fuller, F. D.; Lassalle, L.; Ibrahim, M.; Gul, S.; Fransson, T.; Brewster, A. S.; Alonso-Mori, R.; Hussein, R.; Zhang, M.; Douthit, L.; de Lichtenberg, C.; Cheah, M. H.; Shevela, D.; Wersig, J.; Seuffert, I.; Sokaras, D.; Pastor, E.; Weninger, C.; Kroll, T.; Sierra, R. G.; Aller, P.; Butryn, A.; Orville, A. M.; Liang, M.; Batyuk, A.; Koglin, J. E.; Carbajo, S.; Boutet, S.; Moriarty, N. W.; Holton, J. M.; Dobbek, H.; Adams, P. D.; Bergmann, U.; Sauter, N. K.; Zouni, A.; Messinger, J.; Yano, J.; Yachandra, V. K. Structures of the Intermediates of Kok's Photosynthetic Water Oxidation Clock. *Nature* **2018**, *563*, 421−425.

(115) Ermakova-Gerdes, S.; Yu, Z.; Vermaas, W. Targeted Random Mutagenesis To Identify Functionally Important Residues in the D2 Protein of Photosystem II in *Synechocystis* sp. Strain PCC 6803. *J. Bacteriol.* **2001**, *183*, 145−154.

(116) Adamo, C.; Barone, V. Toward Reliable Density Functional Methods Without Adjustable Parameters: The PBE0 Model. *J. Chem. Phys.* **1999**, *110*, 6158−6170.

(117) Perdew, J. P.; Ernzerhof, M.; Burke, K. Rationale for Mixing Exact Exchange with Density Functional Approximations. *J. Chem. Phys.* **1996**, *105*, 9982−9985.

(118) Grimme, S. Accurate Calculation of the Heats of Formation for Large Main Group Compounds with Spin-Component Scaled MP2 Methods. *J. Phys. Chem. A* **2005**, *109*, 3067−3077.

(119) Alia; Hulsebosch, B.; van Gorkom, H. J.; Raap, J.; Lugtenburg, J.; Matysik, J.; de Groot, H. J. M.; Gast, P. Probing the Electronic Structure of Tyrosine Radical Y_D in Photosystem II by EPR Spectroscopy Using Site Specific Isotope Labelling in *Spirodela oligorrhiza*. *Chem. Phys.* **2003**, *294*, 459−469.

(120) Dole, F.; Diner, B. A.; Hoganson, C. W.; Babcock, G. T.; Britt, R. D. Determination of the Electron Spin Density on the Phenolic Oxygen of the Tyrosyl Radical of Photosystem II. *J. Am. Chem. Soc.* **1997**, *119*, 11540−11541.

(121) Engström, M.; Himo, F.; Gräslund, A.; Minaev, B.; Vahtras, O.; Agren, H. Hydrogen Bonding to Tyrosyl Radical Analyzed by Ab Initio g-Tensor Calculations. *J. Phys. Chem. A* **2000**, *104*, 5149−5153.

(122) Brynda, M.; Britt, R. D. Density Functional Theory Calculations on the Magnetic Properties of the Model Tyrosine Radical-Histidine Complex Mimicking Tyrosyl Radical Y_D·. *Res. Chem. Intermed.* **2007**, *33*, 863−883.

(123) Wang, Y.-N.; Eriksson, L. A. B3LYP Studies of the Formation of Neutral Tyrosyl Radical $Y_{Z\cdot}$ and Regeneration of Neutral Tyrosine Y_Z in PSII. *Int. J. Quantum Chem.* **2001**, *83*, 220−229.

(124) Benisvy, L.; Bittl, R.; Bothe, E.; Garner, C. D.; McMaster, J.; Ross, S.; Teutloff, C.; Neese, F. Phenoxyl Radicals Hydrogen-Bonded to Imidazolium: Analogues of Tyrosyl D· of Photosystem II: High-

Field EPR and DFT Studies. *Angew. Chem., Int. Ed.* **2005**, *44*, 5314−5317.

(125) Nick, T. U.; Lee, W.; Koßmann, S.; Neese, F.; Stubbe, J.; Bennati, M. Hydrogen Bond Network between Amino Acid Radical Intermediates on the Proton-Coupled Electron Transfer Pathway of E. coli α2 Ribonucleotide Reductase. *J. Am. Chem. Soc.* **2015**, *137*, 289−298.

(126) Argirević, T.; Riplinger, C.; Stubbe, J.; Neese, F.; Bennati, M. ENDOR Spectroscopy and DFT Calculations: Evidence for the Hydrogen-Bond Network Within α2 in the PCET of E. coli Ribonucleotide Reductase. *J. Am. Chem. Soc.* **2012**, *134*, 17661−17670.

(127) Hart, R.; O'Malley, P. J. A Quantum Mechanics/Molecular Mechanics Study of the Tyrosine Residue, Tyr_D, of Photosystem II. *Biochim. Biophys. Acta, Bioenerg.* **2010**, *1797*, 250−254.

(128) Mezzetti, A.; Maniero, A. L.; Brustolon, M.; Giacometti, G.; Brunel, L. C. A Tyrosyl Radical in an Irradiated Single Crystal of N-Acetyl-l-tyrosine Studied by X-band cw-EPR, High-Frequency EPR, and ENDOR Spectroscopies. *J. Phys. Chem. A* **1999**, *103*, 9636−9643.

(129) Hulsebosch, R. J.; van den Brink, J. S.; Nieuwenhuis, S. A. M.; Gast, P.; Raap, J.; Lugtenburg, J.; Hoff, A. J. Electronic Structure of the Neutral Tyrosine Radical in Frozen Solution. Selective ^{2}H-, ^{13}C-, and ^{17}O-Isotope Labeling and EPR Spectroscopy at 9 and 35 GHz. *J. Am. Chem. Soc.* **1997**, *119*, 8685−8694.

(130) Hoganson, C. W.; Sahlin, M.; Sjöberg, B.-M.; Babcock, G. T. Electron Magnetic Resonance of the Tyrosyl Radical in Ribonucleotide Reductase from Escherichia coli. *J. Am. Chem. Soc.* **1996**, *118*, 4672−4679.

(131) Campbell, K. A.; Peloquin, J. M.; Diner, B. A.; Tang, X.-S.; Chisholm, D. A.; Britt, R. D. The τ-Nitrogen of D2 Histidine 189 is the Hydrogen Bond Donor to the Tyrosine Radical $Y_D^\bullet$ of Photosystem II. *J. Am. Chem. Soc.* **1997**, *119*, 4787−4788.

(132) Teutloff, C.; Pudollek, S.; Keßen, S.; Broser, M.; Zouni, A.; Bittl, R. Electronic Structure of the Tyrosine D Radical and the Water-Splitting Complex from Pulsed ENDOR Spectroscopy on Photosystem II Single Crystals. *Phys. Chem. Chem. Phys.* **2009**, *11*, 6715−6726.

(133) O'Malley, P. J. Hybrid Density Functional Studies of the Oxidation of Phenol−Imidazole Hydrogen-Bonded Complexes: A Model for Tyrosine Oxidation in Oxygenic Photosynthesis. *J. Am. Chem. Soc.* **1998**, *120*, 11732−11737.

(134) O'Malley, P. J.; Ellson, D. ^{1}H, ^{13}C and ^{17}O Isotropic and Anisotropic Hyperfine Coupling Prediction for the Tyrosyl Radical Using Hybrid Density Functional Methods. *Biochim. Biophys. Acta, Bioenerg.* **1997**, *1320*, 65−72.

(135) Nieuwenhuis, S. A. M.; Hulsebosch, R. J.; Raap, J.; Gast, P.; Lugtenburg, J.; Hoff, A. J. Structure of the Y_D Tyrosine Radical in Photosystem II. Determination of the Orientation of the Phenoxyl Ring by Enantioselective Deuteration of the Methylene Group. *J. Am. Chem. Soc.* **1998**, *120*, 829−830.

(136) Rigby, S. E. J.; Nugent, J. H. A.; O'Malley, P. J. The Dark Stable Tyrosine Radical of Photosystem 2 Studied in Three Species Using ENDOR and EPR Spectroscopies. *Biochemistry* **1994**, *33*, 1734−1742.

(137) Warncke, K.; McCracken, J.; Babcock, G. T. Structure of the Y_D Tyrosine Radical in Photosystem II as Revealed by ^{2}H Electron Spin Echo Envelope Modulation (ESEEM) Spectroscopic Analysis of Hydrogen Hyperfine Interactions. *J. Am. Chem. Soc.* **1994**, *116*, 7332−7340.

(138) Schlodder, E.; Çetin, M.; Lendzian, F. Temperature Dependence of the Oxidation Kinetics of Tyr_Z and Tyr_D in Oxygen-Evolving Photosystem II Complexes Throughout the Range from 320 to 5 K. *Biochim. Biophys. Acta, Bioenerg.* **2015**, *1847*, 1283−1296.

(139) Ahmadova, N.; Mamedov, F. Formation of Tyrosine Radicals in Photosystem II Under Far-Red Illumination. *Photosynth. Res.* **2018**, *136*, 93−106.

(140) Manna, P.; LoBrutto, R.; Eijckelhoff, C.; Dekker, J. P.; Vermaas, W. Role of Arg180 of the D2 Protein in Photosystem II Structure and Function. *Eur. J. Biochem.* **2001**, *251*, 142−154.

(141) Ishikita, H.; Knapp, E.-W. Function of Redox-Active Tyrosine in Photosystem II. *Biophys. J.* **2006**, *90*, 3886−3896.